INTERNATIONAL JOURNAL FOR NUMERICAL METHODS IN FLUIDS
Int. J. Numer. Meth. Fluids 2001; **37**: 445–478 (DOI: 10.1002/fld.183)

Unsteady RANS method for surface ship boundary layer and wake and wave field

Shin Hyung Rhee[1] and Fred Stern*,[2]

Iowa Institute of Hydraulic Research, Department of Mechanical Engineering, University of Iowa, Iowa City, IA, USA

SUMMARY

Results are reported of an unsteady Reynolds-averaged Navier–Stokes (RANS) method for simulation of the boundary layer and wake and wave field for a surface ship advancing in regular head waves, but restrained from body motions. Second-order finite differences are used for both spatial and temporal discretization and a Poisson equation projection method is used for velocity–pressure coupling. The exact kinematic free-surface boundary condition is solved for the free-surface elevation using a body-fitted/free-surface conforming grid updated in each time step. The simulations are for the model problem of a Wigley hull advancing in calm water and in regular head waves. Verification and validation procedures are followed, which include careful consideration of both simulation and experimental uncertainties. The steady flow results are comparable to other steady RANS methods in predicting resistance, boundary layer and wake, and free-surface effects. The unsteady flow results cover a wide range of Froude number, wavelength, and amplitude for which first harmonic amplitude and phase force and moment experimental data are available for validation along with frequency domain, linear potential flow results for comparisons. The present results, which include the effects of turbulent flow and non-linear interactions, are in good agreement with the data and overall show better capability than the potential flow results. The physics of the unsteady boundary layer and wake and wave field response are explained with regard to frequency of encounter and seakeeping theory. The results of the present study suggest applicability for additional complexities such as practical ship geometry, ship motion, and maneuvering in arbitrary ambient waves. Copyright © 2001 John Wiley & Sons, Ltd.

KEY WORDS: free-surface; RANS method; unsteady flow

1. INTRODUCTION

Numerical methods for viscous surface ship hydrodynamics have undergone considerable advancement over the last decade especially for Reynolds-averaged Navier–Stokes (RANS) computational fluid dynamics (CFD) methods and steady flow applications for practical

* Correspondence to: Iowa Institute of Hydraulic Research, Department of Mechanical Engineering, University of Iowa, Iowa City, IA 52242, USA.
[1] Currently CFD Engineer, Fluent Inc., Lebanon, NH, USA.
[2] Fax: + 1-319-335-5238; e-mail: frederick-stern@uiowa.edu

Received 2 September 1999
Revised 30 December 2000

Copyright © 2001 John Wiley & Sons, Ltd.

geometries, as evidenced by comparison results at the recent Gothenburg 2000 Workshop on Numerical Ship Hydrodynamics [1] with those from the previous two workshops, CFD Workshop Tokyo [2] and SSPA-CTH-IIHR Workshop on Ship Viscous Flow [3]. Advancements for off-design problems and unsteady flow, although warranted since CFD Workshop Tokyo, are still relatively rare. For off-design yaw and steady turn problems, steady flow methods can still be used and have shown fairly good agreement with data, although issues remain as to resolution of steep and breaking waves and body and wave-induced vortices [4–6]. For unsteady flow problems, studies are very limited partly due to the fact that not all steady flow methods are easily extended to unsteady flow. Ohmori [7] performs simulations of unsteady combined sway and yaw motions as per captive model testing in towing tanks using planar motion mechanisms; however, the free-surface is neglected, i.e. simulations are for the so-called double body zero Froude number problem. Taylor *et al.* [8] and Gentaz *et al.* [9] perform simulations for forced motions, and Sato *et al.* [10] perform simulations for motions in regular head waves. These studies show promising results; however, conditions and results are limited to forces, moments, and motions in the linear regime such that clearly considerably more work is needed.

The present work concerns the development of an unsteady RANS method for simulation of a surface ship advancing in regular head waves, but restrained from body motions. In ship and platform motions theory, the present problem is referred to as the forward speed diffraction problem and plays an important role in current engineering approaches which use frequency domain, linear, potential flow, strip theory assumptions [11]; since, the exciting forces for motions are the solution to the forward speed diffraction problem. This building block problem for unsteady RANS can also be considered as a first step in merging the separate fields of resistance and propulsion and seakeeping and maneuvering.

Unsteady RANS methods have shown success for a wide variety of engineering problems such as turbomachinery [12], forced and natural unsteady flow [13–17], oscillating flow for a nozzle, channel, jet, or cylinder [18,19], and boundary layer and wake response for unsteady external flows [20,21]. Most studies are for two-dimensional flows. Methods have been based on quite different turbulence models, velocity–pressure coupling algorithms, and temporal and spatial discretization schemes. The best results are for conditions for which unsteady RANS most justified, i.e. forced unsteady flows with periodic mean flow fluctuations in which phase averaging was used as long as time scales of turbulent and mean flow fluctuations differ by several orders of magnitude. The best numerical methods are second-order accurate in both time and space. To date, no consensus has yet been reached with regard to turbulence modeling for unsteady flows.

Free-surface flow methods have been developed for problems related to motions in containers, coastal regions, offshore structures, and ship hydrodynamics. Methods are categorized as (a) mixed Eulerian–Lagrangian [11], (b) spectral [22], and (c) volume discretization. The former have limited applicability to the present problem of viscous ship hydrodynamics. The latter can be further decomposed into surface capturing and tracking approaches. Surface capturing methods [23] are robust in handling complicated geometries with large surface deformations; however, their implementation is usually low-order in its description of the free-surface and computationally intensive for three-dimensional applications. Nonetheless, recent work for ship hydrodynamics [24,25] indicates promise for these methods. For high

Copyright © 2001 John Wiley & Sons, Ltd.

resolution, non-linear, free-surface flows, surface tracking methods thus far have shown best results. Different free-surface conforming grid update techniques have been employed for surface tracking methods: sliding up and down along initial grid lines in the vertical direction [26,28]; redistributing grid points based on the background grid [27]; and regenerating grids based on displacements of the free-surface and the restraints on other boundaries [29]. The basic idea is, however, the same, and the simplest approach, i.e. sliding along initial grid lines, is deemed to be the most efficient one, considering computational resources. Also, use of separate wave adapted grids for solution of the wave elevation equation, has, in some cases, shown an advantage for steady-flow applications [28,29].

The present approach for simulating the forward speed diffraction problem combines the better methods for unsteady RANS with an earlier successful approach for steady flow ship hydrodynamics [28]. The focus is on the development of the overall numerical method and assessment of its capability through application to the model problems of the Wigley hull in calm water (steady flow) and regular head waves (forward speed diffraction problem). Simulations are conducted for a wide range of conditions for which experimental data are available for validation. For steady flow, comparisons are made with data for wave profile [30] and resistance [30,31]. For unsteady flow, comparisons are also made with the linear potential flow method of Kring *et al*. [11]. The Wigley hull (Figure 1) has long been accepted as an international standard albiet simplified ship geometry for CFD code development. The approach also includes consideration of uncertainty assessment, i.e. verification and validation (V&V). More emphasis is being placed on V&V, as CFD matures towards a practical design tool. Although consensus has not yet been reached, one of the methods under consideration is the comprehensive approach of Stern *et al*. [32], which was used at the recent Gothenburg 2000 Workshop on Numerical Ship Hydrodynamics. This present work was used in the development of this method and therefore follows this approach.

The paper is organized as follows. Section 2 describes the model problems, mathematical formulation, and modeling assumptions, and conditions for simulations are also discussed. Section 3 provides detailed documentation for the numerical methods for temporal and spatial discretization, velocity–pressure coupling, free-surface boundary conditions, and overall solution procedure. Section 4 provides an overview of the V&V methodology. Sections 5 and 6 discuss the results for steady and unsteady flow respectively. Discussions focus on performance of the numerical methods, including levels of V&V for both steady and unsteady flow, physics of forward speed diffraction problem, and comparisons with frequency domain, linear potential flow method. Lastly, Section 7 provides some concluding remarks concerning future code development and experimental studies.

2. MODEL PROBLEMS AND MATHEMATICAL FORMULATION AND MODELING

The Wigley hull advancing in calm water and in regular head waves are selected as model problems. Both the standard and modified Wigley hulls are considered for steady flow, while only the modified Wigley hull is considered for unsteady flow due to the availability of experimental data for validation. The standard Wigley hull is a simplified practical geometry,

Copyright © 2001 John Wiley & Sons, Ltd.

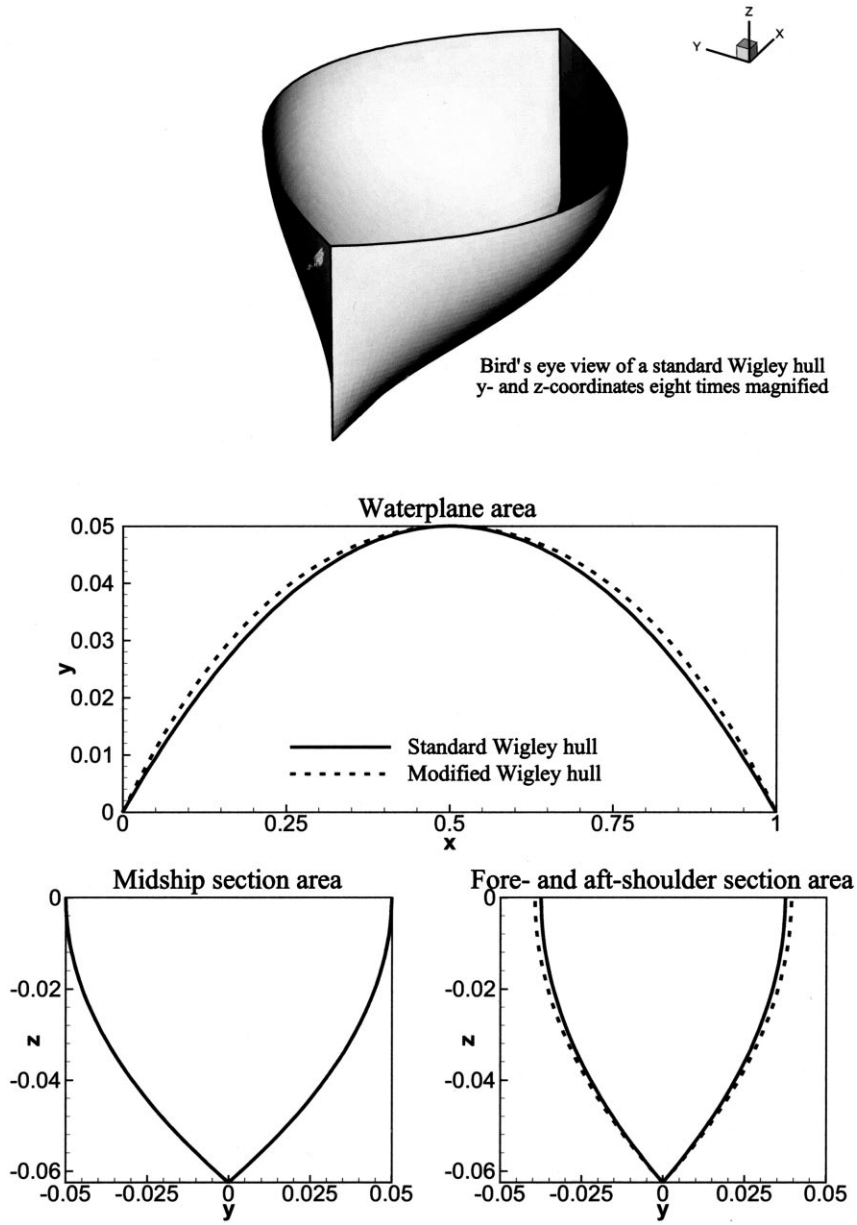

Figure 1. Standard and modified Wigley hull.

Copyright © 2001 John Wiley & Sons, Ltd.

which resembles a canoe. It has been used in many experimental and computational studies. The modified Wigley hull, which is called Wigley III and closest to the standard Wigley hull among four modified hull forms in Journée [31], has fuller shape around the fore- and aft-shoulders. The block coefficients ($C_B = \nabla/LBT$, where ∇ is the displacement volume; L is the length; B is the breadth; and T is the draft of a ship hull) of the standard and modified Wigley hulls are 0.444 and 0.462 respectively, whereas the midship section is the same for both hulls. Figure 1 shows both the standard and modified Wigley hulls.

First, consider a Wigley hull advancing in calm water. Turbulent flow is considered for both the standard and modified Wigley hulls. The (Re, Fr), where Reynolds number, $Re = U_0 L/\nu$, and Froude number, $Fr = U_0/\sqrt{gL}$, are defined in terms of characteristic velocity U_0, L, kinematic viscosity ν, and gravitational acceleration g, for the standard Wigley hull are (3.6×10^6, 0.316), while (Re, Fr) for the modified Wigley hull are (3.24×10^6, 0.2), (4.86×10^6, 0.3), and (6.48×10^6, 0.4). Experimental data from McCarthy [30] and Journée [31] are used for comparison and validation for the standard and modified Wigley hull respectively. Note that experimental data for fixed condition (i.e. no sinkage and trim allowed) are available from McCarthy [30], while Journée [31] reported, for steady flow, data for free sinkage and trim.

Next, consider the modified Wigley hull advancing in regular head waves. As shown in Figure 2, a moving co-ordinate system is adopted that is fixed to the body with x positive downstream, y positive in the starboard direction, and z positive upward. The origin is located at the intersection of bow and undisturbed water level, and the co-ordinates are normalized by L. This co-ordinate system is employed for all calculations in the present study. The computational condition matrix covers a wide range of ($3.24 \times 10^6 \leq Re \leq 6.48 \times 10^6$), ($0.2 \leq Fr \leq 0.4$), ($0.5 \leq \lambda \leq 1.5$), and ($1/190 \leq A/\lambda \leq 1/60$), where λ and A are non-dimensional wavelength and amplitude respectively, based on Journée [31], as presented in Table I. The following abbreviations are used to represent the cases with various computational conditions in this paper: cases for low, medium, and high Froude number (LF, MF, and HF); cases for

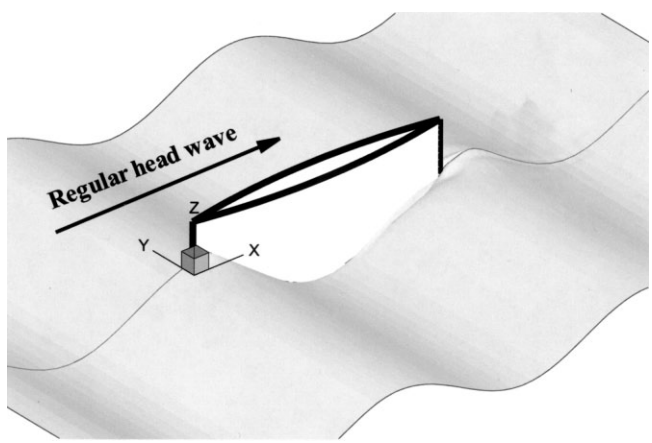

Figure 2. Wigley hull advancing in regular head waves.

Copyright © 2001 John Wiley & Sons, Ltd.

Table I. Computational conditions for the modified Wigley hull advancing in regular head waves.

CASE	Fr	Re	λ	A	A/A_{std}	A/λ	Ak	ξ_e	ω_e (Hz)
LF, ML, SA	0.2	3.24×10^6	1.0	0.0084	1.12	1/119	0.053	18.82	1.083
MF, SL, SA	0.3	4.86×10^6	0.5	0.0082	0.68	1/62	0.10	24.38	2.105
BASE MF, ML, SA	0.3	4.86×10^6	1.0	0.0082	0.68	1/122	0.052	14.64	1.264
MF, ML, MA	0.3	4.86×10^6	1.0	0.0155	1.28	1/65	0.10	14.64	1.264
MF, LL, SA	0.3	4.86×10^6	1.5	0.0078	0.64	1/192	0.033	11.00	0.951
HF, ML, SA	0.4	6.48×10^6	1.0	0.0087	0.51	1/115	0.055	12.55	1.445

short, medium, and long wavelength (SL, ML, and LL); cases for small and medium wave amplitude (SA and MA). The case for large wave amplitude was not considered due to the extreme non-linearity in wave forms, which cannot be resolved by the present CFD method. The BASE case is chosen for MF, ML, and SA, i.e. the median and representative case.

A regular head wave is defined as a progressive wave traveling at steady speed in the positive x-direction such that the combined flow, i.e. body boundary layer and wake and regular head wave external flow, is unsteady. Non-dimensionalized free-surface elevation (ζ), velocity components (U_i), and pressure (p) are written for regular head wave external flow as

$$\zeta(x, t) = A\cos(kx - \xi_e t) \tag{1}$$

$$U(x, z, t) = 1 + \xi A\, e^{kz}\cos(kx - \xi_e t) \tag{2}$$

$$W(x, z, t) = \xi A\, e^{kz}\sin(kx - \xi_e t) \tag{3}$$

$$p(x, z, t) = \frac{\xi^2 A}{k} e^{kz}\cos(kx - \xi_e t) - \frac{(\xi A)^2}{2} e^{2kz} \tag{4}$$

where k is the wave number ($=2\pi/\lambda$), ξ is the wave frequency and ξ_e is the encounter frequency ($=\xi + k$) due to the relative velocity. The profiles of free-surface elevation (ζ), velocity components (U and W), pressure, and pressure gradients ($\partial p/\partial x$ and $\partial p/\partial z$) for $\lambda = 1$ at $t = 0T$ and $T/2$ are displayed in Figure 3. Note that, at $t = 0T$: (a) crests of ζ and p are at bow and stern, whereas trough is at midship; (b) U is maximum and minimum at wave crest and trough respectively; (c) W is upward and downward over the fore- and aft-half of the hull respectively; and (d) U and W directly respond to $\partial p/\partial x$ and $\partial p/\partial z$ respectively, as viscous effect is zero.

The governing equations for the present study are the continuity and RANS equations for viscous incompressible flow written in the physical domain using Cartesian co-ordinates (x, y, z). Using tensor notation, the equations are written as

$$\frac{\partial U_i}{\partial x^i} = 0 \tag{5}$$

Copyright © 2001 John Wiley & Sons, Ltd.

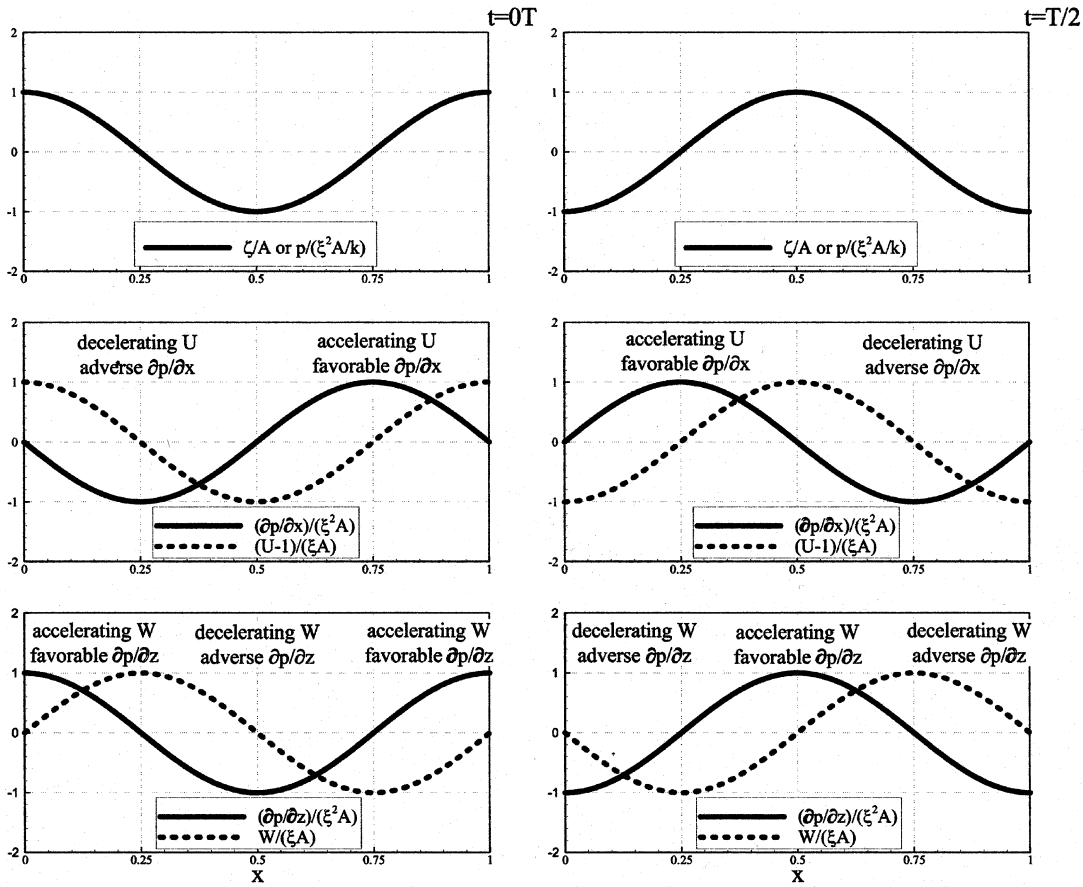

Figure 3. Regular head wave external flow: at $t = 0T$ (left); at $t = T/2$ (right).

$$\frac{\partial U_i}{\partial t} + U_j \frac{\partial U_i}{\partial x^j} + \frac{\partial p}{\partial x^i} - \frac{1}{Re} \nabla^2 U_i - \frac{\partial}{\partial x^j}(-\overline{u_i u_j}) = 0 \tag{6}$$

where

$$\nabla^2 = \frac{\partial^2}{\partial x^j \, \partial x^j}$$

and $U_i = (U, V, W)$ are the Cartesian components of velocity normalized by U_0, $x^i = (x, y, z)$ are the non-dimensional co-ordinates normalized by L, p $(= p_{\text{static}} + \rho g z)$ is the piezometric pressure normalized by ρU_0^2.

Copyright © 2001 John Wiley & Sons, Ltd.

Most unsteady RANS methods (as referenced earlier) have used usual zero-, one-, and two-equation turbulence models developed for steady flows without modifications for unsteady flow. Some limited studies have been done on evaluation and/or development of turbulence models specifically for unsteady flows, but investigations are limited to two-dimensional applications [33–35]. In view of the current situation for turbulence modeling for unsteady flows and the present focus on development of an overall numerical method, the widely used standard Baldwin–Lomax turbulence model is adopted [36].

The solution domain is shown in Figure 4, which is a quarter-cylinder with extent $-1 \le x \le 2$, $0 \le r \le 1$, $0 \le \theta \le \pi/2$, where $r = \sqrt{y^2 + z^2}$ and $\theta = \tan(-y/z)$. The influence of the solution domain size was studied as part of the verification study and presented in Rhee [37]. The boundary condition on each boundary is: (a) on the inlet plane S_i, U, V, W, and p are specified from the external flow values, i.e. uniform stream or regular head wave external flow; (b) on the body surface S_b, the no-slip condition is imposed; (c) on the symmetry planes S_{cp}, $\partial(U, W, p)/\partial y = V = 0$; (d) on the outer boundary S_o, $\partial(U, V, W, p)/\partial n = 0$; (e) on the free-surface S_ζ, the kinematic and dynamic conditions are satisfied, which are formulated and restricted herein for a continuous interface without wave breaking or free-surface turbulence; and (f) on the exit plane, S_e, $\partial^2(U, V, W, p)/\partial x^2 = 0$ for steady flow or $\partial^2[(U - U_e), V, (W - W_e), (p - p_e)]/\partial x^2 = 0$ for unsteady flow, in which U_e, W_e, and p_e are from the inviscid outer flow, i.e. incident wave without viscous flow effects. Note that the zero-diffusion condition on S_e, i.e. the physical interpretation of $\partial^2[(U - U_e), V, (W - W_e), (p - p_e)]/\partial x^2 = 0$, is valid for forced unsteady flow, since $(U - U_e)$, $(W - W_e)$, and $(p - p_e)$ retain viscous wake effects throughout the exit plane.

The kinematic free-surface boundary condition expresses the requirement that the free-surface is a stream surface, and the dynamic free-surface boundary condition requires that the stress is continuous across S_ζ, where, in general, the effects of outer air and surface tension are included. Herein, however, the effects of outer air and surface tension are assumed to be zero, i.e.

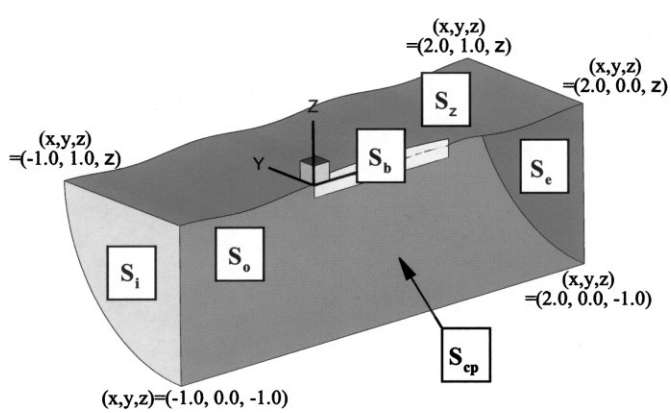

Figure 4. Solution domain.

Copyright © 2001 John Wiley & Sons, Ltd.

$$\tau_{ij} n_j = 0 \tag{7}$$

where

$$\tau_{ij} = -\left(p - \frac{\zeta}{Fr^2}\right)\delta_{ij} + \frac{1}{Re}\left(\frac{\partial U_i}{\partial x^j} + \frac{\partial U_j}{\partial x^i}\right) - \overline{u_i u_i}$$

and

$$n_j = \frac{(\partial\zeta/\partial x,\ \partial\zeta/\partial y,\ -1)}{\sqrt{(\partial\zeta/\partial x)^2 + (\partial\zeta/\partial y)^2 + 1}}$$

and the gradients of S_ζ and W in tangential directions, i.e. $\partial\zeta/\partial x$, $\partial\zeta/\partial y$, $\partial W/\partial x$ and $\partial W/\partial y$, are assumed to be small, thereby the approximate dynamic condition ($\partial U/\partial z = 0$, $\partial V/\partial z = 0$, and $p = \zeta/Fr^2$) is used with $\partial W/\partial z = -\partial U/\partial x - \partial V/\partial y$, which ensures the kinematic free-surface boundary condition, i.e. no flow across the free-surface. It should be noted that, since the dynamic condition does not contain temporal terms and is satisfied in each time step, the approximation has no influences on the time accuracy of solutions.

The initial condition is the values from the uniform stream (i.e. $U = 1$, $V = W = p = 0$) for a Wigley hull advancing in calm water, while the sum of the steady flow solution and values of the external flow is given as initial condition for a Wigley hull advancing in regular head waves.

3. NUMERICAL METHOD

A numerical method was developed and implemented in a computer code for the solution of the unsteady RANS mathematical formulation and modeling described in the previous section. Although the method retains certain features of its predecessor [28], i.e. incompressible flow mathematical formulation and approach for free-surface boundary conditions, the underlying methodology is different. In particular, second-order finite differences are used for spatial discretization (versus finite analytic method) and a Poisson equation projection method is used for velocity–pressure coupling (versus PISO algorithm). These changes were deemed necessary for improved order of accuracy, especially in inviscid regions, and for faster convergence that is lacking in the predecessor and crucial for unsteady flow calculations.

The RANS equations are transformed from the physical domain in Cartesian co-ordinates (x, y, z, t) into the computational domain in generalized curvilinear co-ordinates (ξ, η, ζ, τ). A partial transformation is used in which only the independent variables are transformed, leaving the velocity components U_i in Cartesian co-ordinates. Using the co-ordinate transformation relations, the governing equations (5) and (6) are written as

$$\frac{1}{J}\frac{\partial}{\partial\xi^j}(JU^j) = \frac{1}{J}\frac{\partial}{\partial\xi^j}(b_i^j U_i) = 0 \tag{8}$$

Copyright © 2001 John Wiley & Sons, Ltd.

$$\frac{\partial U_i}{\partial \tau} - \frac{1}{J} b_i^j \frac{\partial x^i}{\partial \tau} \frac{\partial U_i}{\partial \xi^j} + U^k \frac{\partial U_i}{\partial \xi^k} = -\frac{1}{J} b_i^k \frac{\partial p}{\partial \xi^k} + \frac{1}{R_{\text{eff}}} \nabla^2 U_i + \left(\frac{1}{J} b_j^k \frac{\partial v_t}{\partial \xi^k}\right)\left[\left(\frac{1}{J} b_t^l \frac{\partial U_j}{\partial \xi^l}\right) + \left(\frac{1}{J} b_j^l \frac{\partial U_i}{\partial \xi^l}\right)\right] \tag{9}$$

where b_i^j and g^{ij} are geometric coefficients, J is Jacobian, and the contravariant velocity component is defined by $U^k = (1/J) b_j^k U_j$ and $b_j^l b_j^k = J^2 g^{lk}$ from the relationship of geometric coefficients.

The second-order finite difference schemes are employed in the discretization of the governing equations. The resulting discretized form of (9) is then, for unsteady flow

$$\begin{aligned} &\frac{3U_i^{n,m} - 4U_i^{n-1} + U_i^{n-2}}{2\Delta\tau} - \frac{1}{J} b_i^j \frac{3x^{i,n,m-1} - 4x^{i,n-1} + x^{i,n-2}}{2\Delta\tau} \delta_{\xi^k}(U_i^{n,m}) \\ &\quad + \frac{1}{2}(U^k + |U^k|)^{n,m-1} \delta_{\xi^k}^{-2}(U_i^{n,m}) - \frac{1}{2}(U^k - |U^k|)^{n,m-1} \delta_{\xi^k}^{+2}(U_i^{n,m}) \\ &= -\frac{1}{J} b_i^k \delta_{\xi^k}(p^{n,m}) + \frac{1}{R_{\text{eff}}} [g^{kk} \tilde{\delta}_{\xi^k}(\tilde{\delta}_{\xi^k}(U_i^{n,m})) + g^{jk} \delta_{\xi^l}(\delta_{\xi^j}(U_i^{n,m-1})) + f^k \delta_{\xi^k}(U_i^{n,m})] \\ &\quad + \left(\frac{1}{J} b_j^k \delta_{\xi^k}(v_t)^{n,m-1}\right)\left[\frac{1}{J} b_i^l \delta_{\xi^l}(U_j^{n,m-1}) + \left(\frac{1}{J} b_j^l \delta_{\xi^l}(U_i^{n,m-1})\right)\right] \end{aligned} \tag{10}$$

where $\delta_{\xi^k}^{-2}$, $\delta_{\xi^k}^{+2}$, δ_{ξ^k}, and $\tilde{\delta}_{\xi^k}$, indicate the second-order backward, forward, central, and half-interval central discretization operators respectively. Also, $\Delta\tau$ is the time step size and superscripts '$n-2$', '$n-1$', and 'n' represent two previous and present time steps respectively, while superscripts '$m-1$' and 'm' denote the previous and present subiteration steps respectively. For unsteady flows, the second term on the left-hand side takes into account of grid velocity $\partial x^i/\partial\tau$, since the grid conforms to the wave and body in each time step. The discretized momentum transport equations are solved using a Peaceman–Rachford type alternate direction implicit (ADI) method.

A Poisson equation projection method is used for velocity–pressure coupling. The method is based on Harlow and Welch [38] with modifications for use of a regular grid system [39]. The discretized pressure Poisson equation is written as

$$\frac{\partial}{\partial \xi^j}\left(J\Delta\tau g^{jk} \frac{\partial p^{n,m}}{\partial \xi^k}\right) = \frac{\partial}{\partial \xi^j}(b_i^j U_i^{n,m-1}) \tag{11}$$

In order to avoid oscillations in the pressure field, fourth-order artificial dissipation is added implicitly, i.e. the term on the left-hand side of (11) is approximated using the combination of δ_{ξ^k}, and $\tilde{\delta}_{\xi^k}$ as

$$\frac{\partial}{\partial \xi^j}\left(J\Delta\tau g^{jk} \frac{\partial p^{n,m}}{\partial \xi^k}\right) \cong (1-\gamma) L p^{n,m} + \gamma \tilde{L} p^{n,m} + N p^{n,m} \tag{12}$$

Copyright © 2001 John Wiley & Sons, Ltd.

where, for a scalar variable φ

$$L\varphi = J\Delta\tau g^{ij}\frac{\varphi_{j-2} - 2\varphi_j + \varphi_{j+2}}{4}$$

$\tilde{L}\varphi = J\Delta\tau g^{ij}(\varphi_{j-1} - 2\varphi_j + \varphi_{j+1})$ and

$$N\varphi = J\Delta\tau g^{jk}\frac{-\varphi_{j-1} + \varphi_{j+1} - \varphi_{k-1} + \varphi_{k+1}}{4}$$

and γ of 0.1 is a dissipation parameter, which is the minimum amount to eliminate the oscillation. γ of 0 results in a one-interval formulation with an oscillating pressure field and γ of 1 results in a half-interval formulation with the artificial dissipation of

$$\frac{1}{4}(J\Delta\tau g^{ij})\frac{\partial^4 p}{\partial\xi^{j4}}$$

approximately. By discretizing the term on the right-hand side of (11) using $\delta_{\xi k}$, the final form of the discretized pressure Poisson equation is written as

$$(1-\gamma)Lp^{n,m} + \gamma\tilde{L}p^{n,m} + Np^{n,m} = \delta_{\xi j}(b_i^j U_i^{n,m-1}) \tag{13}$$

and (13) is solved using a penta-diagonal matrix solver.

The free-surface boundary conditions are implemented as follows: the dynamic free-surface boundary condition presented in the previous section is used as boundary conditions for p and U_i. The kinematic free-surface condition is then used to solve for ζ in each time step. The procedure for solving the kinematic free-surface boundary condition and adjusting grids are adopted from Tahara and Stern [28]. The kinematic free-surface boundary condition is written as, considering grid velocity $\partial x_g/\partial t$ and $\partial y_g/\partial t$

$$\frac{\partial\zeta}{\partial t} + \frac{\partial\zeta}{\partial x}\frac{\partial x_g}{\partial t} + \frac{\partial\zeta}{\partial y}\frac{\partial y_g}{\partial t} + U\frac{\partial\zeta}{\partial x} + V\frac{\partial\zeta}{\partial x} - W = 0 \tag{14}$$

Transforming (14) into computational domain results in

$$\frac{\partial\zeta}{\partial\tau} + \tilde{U}\frac{\partial\zeta}{\partial\xi} + \tilde{V}\frac{\partial\zeta}{\partial\eta} - W = 0 \tag{15}$$

where

$$\tilde{U} = \frac{1}{J}\left[b_1^1\left(U + \frac{\partial x_g}{\partial t}\right) + b_2^1\left(V + \frac{\partial y_g}{\partial t}\right)\right]$$

and

Copyright © 2001 John Wiley & Sons, Ltd.

$$\tilde{V} = \frac{1}{J}\left[b_1^2\left(U + \frac{\partial x_g}{\partial t} \right) + b_2^2\left(V + \frac{\partial y_g}{\partial t} \right) \right]$$

Equation (15) is then solved using the Beam and Warming linear-multistep method based on space-centered finite differences, approximate factorization, and the addition of both implicit and explicit fourth-order artificial dissipation. For unsteady flow calculations in which subiteration is employed, pseudo-time step $\Delta\tau^*$ is introduced and (15) is rewritten as

$$\frac{\partial \zeta}{\partial \tau^*} + \frac{\partial \zeta}{\partial \tau} + \tilde{U}\frac{\partial \zeta}{\partial \xi} + \tilde{V}\frac{\partial \zeta}{\partial \xi} - W = 0 \tag{16}$$

or

$$\zeta^{n,m} = \zeta^{n,m-1} - \frac{\Delta\tau^*}{2}\left[\left(\tilde{U}\frac{\partial \zeta}{\partial \xi} + \tilde{V}\frac{\partial \zeta}{\partial \eta} - W + \frac{\partial \zeta}{\partial \tau} \right)^{n,m-1} + \left(\tilde{U}\frac{\partial \zeta}{\partial \xi} + \tilde{V}\frac{\partial \zeta}{\partial \eta} - W + \frac{\partial \zeta}{\partial \tau} \right)^{n,m} \right] \tag{17}$$

Once convergence is obtained, $\partial\zeta/\partial\tau^*$ is nearly zero and (15) is satisfied at the end of each physical time step. By introducing the delta from such that $\Delta\zeta^{n,m} = \zeta^{n,m} - \zeta^{n,m-1}$ and the differential operator D, (17) reduces to

$$D[\Delta\zeta^{n,m}] = \Delta\tau^*\left(-\tilde{U}\frac{\partial \zeta}{\partial \xi} - \tilde{V}\frac{\partial \zeta}{\partial \xi} + W - \frac{\partial \zeta}{\partial \tau} \right)^{n,m} \tag{18}$$

where

$$D = \left[1 + \frac{\Delta\tau^*}{2}\left(\tilde{U}^{n,m}\frac{\partial}{\partial \xi} + \tilde{V}^{n,m}\frac{\partial}{\partial \eta} \right) \right]$$

If D is factored into two one-dimensional operators, (18) becomes

$$D_1[\Delta\zeta^{n,m}] \cdot D_2[\Delta\zeta^{n,m}] = \Delta\tau^*\left(-\tilde{U}\frac{\partial \zeta}{\partial \xi} - \tilde{V}\frac{\partial \zeta}{\partial \mu} + W - \frac{\partial \zeta}{\partial \tau} \right)^{n,m} \tag{19}$$

where

$$D_1 = \left[1 + \frac{\Delta\tau^*}{2}\frac{\partial}{\partial \xi}(\tilde{U})^{n,m} \right]$$

and

$$D_2 = \left[1 + \frac{\Delta\tau^*}{2}\frac{\partial}{\partial \xi}(\tilde{V})^{n,m} \right]$$

Copyright © 2001 John Wiley & Sons, Ltd.

Equation (19) can now be solved in two one-dimensional inversions and both implicit and explicit fourth-order artificial dissipation terms are added to damp out oscillations and/or maintain stability, such that

$$D_1^*[\Delta\zeta'] = \Delta\tau^*\left(-\tilde{U}\frac{\partial\zeta}{\partial\xi} - \tilde{V}\frac{\partial\zeta}{\partial\eta} + W - \frac{\partial\zeta}{\partial\tau} - \alpha\frac{\partial^4\zeta}{\partial\xi^4} - \alpha\frac{\partial^4\zeta}{\partial\eta^4}\right)^{n,m} \tag{20}$$

$$D_2^*[\Delta\zeta^{n,m}] = \Delta\zeta' \tag{21}$$

where

$$D_1^* = \left[1 + \frac{\Delta\tau^*}{2}\frac{\partial}{\partial\xi}(\tilde{U})^{n,m} + \alpha\frac{\partial^4\zeta}{\partial\xi^4}\right], \qquad D_2^* = \left[1 + \frac{\Delta\tau^*}{2}\frac{\partial}{\partial\xi}(\tilde{V})^{n,m} + \alpha\frac{\partial^4\zeta}{\partial\eta^4}\right]$$

and

$$\frac{\partial\zeta^{n,m}}{\partial\tau} = \frac{\zeta^{n,m} - \zeta^{n,m-1}}{\Delta\tau}$$

The parameter for the artificial dissipation (α) is 0.4 and local time stepping is used with $\Delta\tau^* = 0.1\Delta\tau\sqrt{U^2 + V^2 + W^2}$. The value of α ($= 0.4$) is based on a parametric study with laminar flow around a surface-piercing flat plate advancing in calm water. When α is too small (< 0.04), the free-surface elevation is unstable and shows wiggles, while with too large α (> 4.0), free-surface becomes overly smooth. Equations (20) and (21) are solved using a penta-diagonal matrix solver with the following boundary conditions: on the inlet boundary, $\Delta\zeta = 0$; on the exit boundary, $\Delta\zeta = ax^2 + c$; on the body and centerline boundaries, $\Delta\zeta = ay^2 + c$; and on the outer boundary, $\partial(\Delta\zeta)/\partial y = 0$. Finally, to accurately resolve both the wave and velocity fields, the kinematic free-surface boundary condition is solved on a two-dimensional grid generated separately from, but coupled to, the RANS grid, i.e. velocity field on the free-surface is interpolated into the free-surface grid and the resulting free-surface elevation is interpolated into the RANS grid using bi-linear interpolation. Since the kinematic free-surface boundary condition is treated as a standard advection equation with source terms for the x–y plane, the two-grid method does not affect mass and momentum conservation, which is ensured in the RANS grid, or time accuracy of the solution.

H-type grids with constant-x planes are stacked to form a complete three-dimensional grid. The constant-x plane grids for a Wigley hull are generated by solving a Poisson equation elliptically. The kinematic free-surface boundary condition grid is updated iteratively to fit the wave-body intersection, and is different from the viscous flow grid in that instead of high near-well resolution, more points are distributed in the external flow to resolve the wave field.

The overall solution procedure is summarized as:

1. Input: grids, parameters, and initial condition.
2. Conform grid at the beginning of calculation using initial condition.
3. Set initial guess for U_t, p, and ζ at the present time step.

Copyright © 2001 John Wiley & Sons, Ltd.

4. Set boundary conditions for the present time step.
5. Conform grid and calculate geometric coefficients.
6. Calculate v_t.
7. Calculate finite difference coefficients.
8. Calculate source terms and mass source for the pressure equation.
9. Solve for p, i.e. pressure Poisson equation.
10. Solve for U_i, i.e. momentum equations.
11. Solve for ζ, i.e. kinematic free-surface boundary condition.
12. Update variables for next subiteration.
13. Check if convergence criterion is reached for U_i and p, if not, go to (5) for next subiteration.
14. Store U_i, p, and v_t for the present time step, and, during the last period, output for unsteady flow calculation.
15. Go to (3) for the next time step.
16. Output for steady flow calculation

A subiteration loop (i.e. steps 3 through 13) is introduced in each time step for unsteady flow calculation. The solution at the present time step is updated in the subiteration loop until the residuals of p and U_i between subiteration steps reach the given convergence criterion, which is determined based on the iterative convergence study. For steady flow calculation, subiteration is not employed and therefore steps 3, 4, 12, and 13 are omitted.

In order to implement the subiteration efficiently, an initial guess of p, U_i, and ζ, which is in part based on potential flow calculation method, is given at the beginning of each time step (step 3). An initial guess is the sum of external flow at the present time step and the disturbance due to a surface-piercing body, which has been accumulated from the beginning of the calculation. The initial guess of ζ, for example, is given by $\zeta^n_{\text{initial}} = \zeta^n_{\text{e}} + (\zeta^{n-1}_{\text{e}} - \zeta^{n-1})$, where superscripts '$n-1$' and '$n$' denote the previous and present time steps respectively, while subscripts 'initial' and 'e' represent the initial guess and external flows respectively. Since the solution at the present time step is obtained implicitly by using the solutions at two previous time steps and the boundary conditions, the initial guess does not affect the final solution at the end of each time step.

In steps 9 through 11, the boundary conditions set in step 4 are imposed and an underrelaxation factor of 0.1 is employed. The solution of unsteady flow calculation is saved in step 14 (for the last period only), whereas the output for steady flow calculation is done in step 16 (i.e. at the end of the calculation).

4. UNCERTAINTY ASSESSMENT

To assure high-quality solutions, quantification of errors and uncertainties is a requirement for all CFD simulations. A brief review of uncertainty assessment procedures proposed by Stern *et al.* [32] is presented next and followed by application to the present model problems. The CFD V&V procedures to estimate the errors and uncertainties can be conveniently grouped in four consecutive steps. The first step is preparation, which involves selection of the CFD code

Copyright © 2001 John Wiley & Sons, Ltd.

and specification of objectives, geometry, conditions, and available benchmark data for validation. The objectives might be prediction of certain variables at certain levels of validation. The variables can either be integral (e.g. total drag) or point (e.g. mean velocities) values and the levels of validation may be different for each variable. Sources of errors and uncertainties in results can be divided into two distinct sources: modeling and numerical. Modeling errors and uncertainties are due to assumptions and approximations in the mathematical representation of the physical problem and incorporation of previous data into the model. Numerical errors and uncertainties are due to numerical solution of the mathematical equations. The second step is verification, which is defined as a process for assessing simulation numerical uncertainty U_{SN} and, when conditions permit, estimating the sign and magnitude of the simulation numerical error δ_{SN} and the uncertainty in that error estimate U_{S_cN}. Iterative and parameter convergence studies are conducted using multiple solutions with systematic parameter refinement to estimate numerical uncertainties and/or errors. For converging condition, generalized Richardson extrapolation (RE) is used to estimate uncertainties and, when conditions permit, numerical error itself. For the oscillatory condition, the upper and lower bounds of the solution oscillation are used to estimate uncertainties. The third step is validation, which is defined as a process for assessing simulation modeling uncertainty U_{SM} by using benchmark EFD data and, when conditions permit, estimating the sign and magnitude of the modeling error δ_{SM}. The comparison error E (which is the difference between the data value D and simulation value S) and the validation uncertainty U_V are used in this process. U_V is the combination of all uncertainties in the data and the portion of the simulation uncertainties that can be estimated. Validation is achieved at the U_V level for $|E| < U_V$. When both the magnitude and sign of U_{SN} are estimated, a numerical benchmark is defined by $S_C = S - \delta_{SN}$ and used in the validation process to define E_C and U_{V_C} with validation achieved for $|E_C| < U_{V_C}$. The fourth step is documentation, which is detailed presentation of the code, objectives, geometry, conditions, verification, validation, and analysis.

The present work was used in the development of V&V procedures of Stern *et al.* [32], which are based on extensions of the verification procedures of Stern *et al.* [40] combined with the validation procedures of Coleman and Stern [41]. However, the present work was completed in 1998 such that the uncertainty assessment largely follows the earlier procedures with the exception of the steady flow resistance.

In previous sections, detailed presentation of the CFD code and objectives, geometry, conditions, and available benchmark data are given. In the present section, the verification results are summarized for each of the model problems. The validation results are presented in the following sections in conjunction with the overall steady and unsteady flow results.

First, consider the steady flow. Verification is done for the standard Wigley hull and the results are adopted for the modified hull in the validation procedure without separate verification analyses. This can be justified by the fact that the grid design and important parameters used for the standard Wigley hull are the same for the modified Wigley hull grid and that the difference of hull form is only 3.8 per cent based on C_B. Verification is performed with consideration to iterative and grid convergence studies, i.e. $\delta_{SN} = \delta_I + \delta_G$, where δ_I and δ_G are error contributions from iteration and grid size respectively, and $U_{SN}^2 = U_I^2 + U_G^2$, where U_I and U_G are uncertainty contributions from iteration and grid size respectively. The studies

Copyright © 2001 John Wiley & Sons, Ltd.

Table II. Grid convergence study for the standard Wigley hull advancing in calm water.

Grid	Coarse ($75\times44\times22$)	Medium ($105\times61\times31$)	Fine ($148\times86\times43$)	R_G	p_G	C_G	$\delta_{RE_{G_i}}$	For $\lvert 1-C_G\rvert \gg 1$	For $\lvert C_G\rvert \approx 1$	
								U_G	δ_G	U_G
C_T	5.58×10^{-3}	5.26×10^{-3}	5.11×10^{-3}	0.47	2.17	1.12	2.52% D	3.29% D	2.91% D	0.31% D
ε		-6.2% D	-2.9% D							
$\bar{\varepsilon}[\zeta_{cp}(x)]$ for $0<x<1$		3.7% Fr^2	0.36% Fr^2*	0.097	6.72					

* $\bar{\varepsilon}_{\text{medium-fine}}$ was taken as U_G in the early procedure.

Copyright © 2001 John Wiley & Sons, Ltd.

are conducted for three grids (presented in Table II) with systematic grid refinement ratio $r_G = \sqrt{2}$ in each co-ordinate direction.

The iteration errors and uncertainties are negligible in comparison to the grid errors and uncertainties for all three solutions, i.e. $\delta_I \ll \delta_G$ and $U_I \ll U_G$ such that $\delta_{SN} = \delta_G$ and $U_{SN} = U_G$. The results from the grid convergence study for both the integral, i.e. total resistance coefficient ($C_T = \text{total drag}/\frac{1}{2}\rho S_w U_0^2$, where S_w is the wetted surface area of hull) and point variable, i.e. wave profile (ζ_{cp}), are summarized in Table II. A domain averaging is used for point variables, such that $\bar{\Phi} = (1/\Omega)\int_\Omega \Phi \, d\Omega$ where Φ is any point variable or quantity and Ω is the domain of interest presented with Φ. For example, $\bar{\varepsilon}[\zeta_{cp}(x)]$ for $0 < x < 1$ are domain averaged solution changes $\varepsilon[\zeta_{cp}(x)]$ over the domain $0 < x < 1$. The errors and uncertainties are in percentage of benchmark data (D) for C_T and of Fr^2, a reference range of free-surface wave in steady flow, for $\zeta_{cp}(x)$.

For C_T, the solutions indicate converging condition with the ratio of solution changes ε for medium-fine and coarse-medium grids, $R_G = 0.47$. The order of accuracy p_G, correction factor C_G, and one-term RE estimate $\delta_{RE_{G1}}$ are 2.17, 1.12, and 2.52 per cent D respectively. Uncertainty and error estimates are made both considering C_G as sufficiently less than or greater than one and lacking confidence, and C_G as close to one and having confidence. For $C_G = 1.12$ considered as sufficiently less than or greater than one and lacking confidence, U_G is estimated as 3.29 per cent D and not δ_G. For $C_G = 1.12$ considered close to one and having confidence, both δ_G and U_G are estimated as 2.91 per cent D and 0.31 per cent D respectively. For $\zeta_{cp}(x)$, U_G is obtained from Table II by taking the grid convergence metric between fine and medium grids ($\varepsilon_{fine-medium}$), which are solution changes normalized by Fr^2.

Next, consider the unsteady flow. Among the six cases for variation of Fr, λ, and A, the BASE case is considered for verification analysis. The other cases are not considered for verification, but the numerical uncertainties for the BASE case should be fairly representative except, possibly, the low Fr (LF) and short wavelength (SL) cases. Grid design and important parameters are the same as those for the steady flow. Table III presents the numerical uncertainties for unsteady flow. As for the steady flow, both integral, e.g. surge force coefficient ($F_x = \text{surge force}/\frac{1}{2}\rho S_w U_0^2$), and point, e.g. wave pattern (ζ), variables are considered in verification. The verification results for heave force coefficient ($F_z = \text{heave force}/\frac{1}{2}\rho L^2 U_0^2$) and pitch moment coefficient ($M_y = \text{pitch moment}/\frac{1}{2}\rho L^3 U_0^2$) are not in Table III, but the

Table III. Numerical uncertainties for the modified Wigley hull advancing in regular head waves.

	U_G	U_T	U_{SN}
$F_{x,1}$	1.84% D	1.23% D	2.22% D
$\gamma(F_{x,1})$	−6.21% 2π	−6.22% 2π	6.34% 2π
	$\bar{U}_G$	$\bar{U}_T$	$\bar{U}_{SN}$
$\zeta_1(x, y)$ for $-1 < x < 2$, $0 < y < 1$	0.51% A	0.44% A	0.67% A
$\gamma(\zeta_1(x, y))$ for $-1 < x < 2$, $0 < y < 1$	0.18% 2π	0.12% 2π	0.22% 2π

Copyright © 2001 John Wiley & Sons, Ltd.

values of U_{SN} are presented later in Table VI for validation. The amplitude and phase of first harmonic components are used for iterative, grid, and time-step convergence studies. The uncertainties for the first harmonic amplitudes of F_x and ζ are normalized by benchmark data (D) and incident wave amplitude (A) respectively. The uncertainties for the first harmonic phase are normalized by 2π. U_I is less than $O(10^{-6})$, i.e. negligibly small compared to U_G and the uncertainty in time-step convergence (U_T), and therefore $U_{SN}^2 = U_G^2 + U_T^2$. U_{SN} for the first harmonic amplitudes of F_x and ζ are 2.15 per cent D and 0.67 per cent A respectively, and U_{SN} for the first harmonic phase are 6.34 per cent 2π and 0.22 per cent 2π for F_x and ζ respectively.

Levels of verification for both steady and unsteady flows are acceptable in consideration of grid densities and levels of experimental uncertainties as given in the next sections.

5. STEADY FLOW

The standard hull investigations include validation of the resistance and wave profile through comparison with data [30] and qualitative assessment based on other available CFD results [26,42]. Table IV presents validation results for the standard Wigley hull. For C_T, validation is performed using both simulation (S) and simulation corrected for numerical errors ($S_C = S - C_G\delta_{RE_G}$) and the results are shown for benchmark data (D), S, and S_C, error ($E = D - S$ and $E_C = D - S_C$), validation uncertainty (U_V), uncertainty in data (U_D), and numerical uncertainty (U_{SN}). Since detailed EFD uncertainty assessment is not available from McCarthy [30] and Journée [31], U_D for C_T is assumed to be 2.5 per cent D based on Longo and Stern [43], which documents an extensive survey on EFD uncertainty for various ship hull forms. Validation is achieved, i.e. $|E| < U_V$, using S at the level $U_V = 4.10$ per cent D, but not achieved using S_C. However, note that U_V using S_C is relatively small and U_{SN} is an order of magnitude smaller than U_D, suggesting that $E_C = D - S_C$ is mostly due to modeling errors. Table IV also presents errors and uncertainties for wave profile on hull and centerline, $\zeta_{cp}(x)$. Due to the same reason as for C_T, U_D for $\zeta_{cp}(x)$ is assumed to be 1.25 per cent Fr^2 based on the naval surface warfare center experiment for the Model 5415. The errors and uncertainties for $\zeta_{cp}(x)$ are normalized by Fr^2 (i.e. a reference range of $\zeta_{cp}(x)$ in calm water), since $\zeta_{cp}(x)$ is small and varies across zero. Validation is achieved at the level $\bar{U}_V = 1.30$ per cent Fr^2. The detailed discussion of $\zeta_{cp}(x)$ is presented with Figure 5, which shows comparison with the data and the corresponding E and U_V. The largest differences are observed near the bow and stern, such that the bow wave is underpredicted and slightly shifted aft, while the stern wave including peak value is overpredicted. These differences are due to the finite thickness at the bow of the model and free-surface turbulence effects near the stern in the experiment.

Other CFD studies for the standard Wigley hull [26,42] presented similar trends. C_T was overpredicted by 3 per cent D in Tahara *et al.* [42] and by 5 per cent D in Farmer *et al.* [26], which are similar to the present results. $\zeta_{cp}(x)$ of Tahara *et al.* [42] shows larger under- and overprediction near the bow and stern respectively, than the present result, whereas $\zeta_{cp}(x)$ of Farmer *et al.* [26] shows somewhat better agreement.

The modified hull investigations include validation of the resistance through comparison with data [31], assessment of difference for standard and modified hulls, and the effects of Fr. Table V presents validation results for C_T at three sets of (Re, Fr). As mentioned in Section

Copyright © 2001 John Wiley & Sons, Ltd.

Table IV. Validation for the standard Wigley hull advancing in calm water.

D	S	$E = D - S$	U_V	U_D	U_{SN}	S_C	$E_C = D - S_C$	U_V	U_{SN}
C_T 5.16×10^{-3}	5.11×10^{-3}	0.97% D	4.10% D	2.5% D	3.29% D	4.96×10^{-3}	3.88% D	2.52% D	0.31% D
		$\bar{E} = \overline{D - S}$	$\bar{U}_V$	$\bar{U}_D$	$\bar{U}_{SN}$				
$\zeta_{cp}(x)$ for $0 < x < 1$		0.66% Fr^2	1.30% Fr^2	1.25% Fr^2	0.36% Fr^2				

Copyright © 2001 John Wiley & Sons, Ltd.

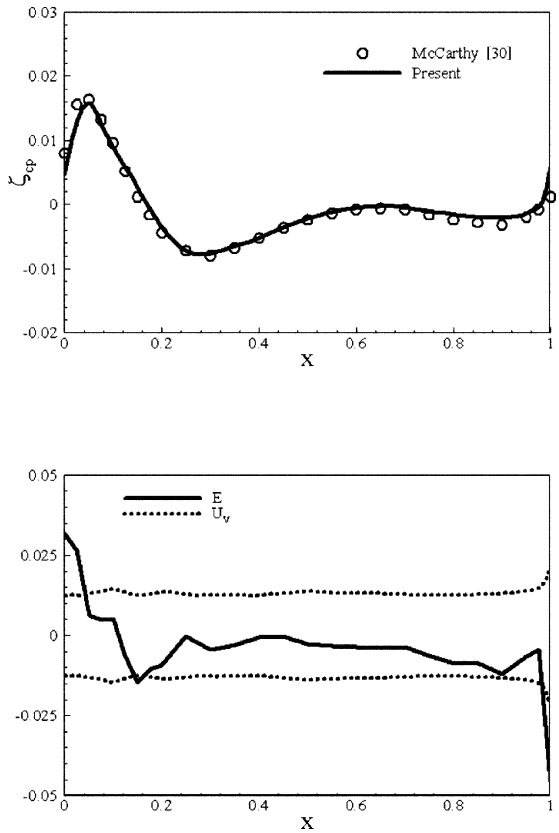

Figure 5. Validation of wave profile for the standard Wigley hull advancing in calm water.

4, the values of U_V, U_D, and U_{SN} for the standard hull are adopted in the validation analysis. Validation is achieved using S at the level $U_V = 3.38$ per cent D to 5.91 per cent D for all three Fr values, and using S_C at the level $U_V = 2.33$ per cent D to 3.02 per cent D for $Fr = 0.2$ and 0.3. $|E|$ and $|E_C|$ are smaller at lower Fr (i.e. lower Re), which is likely due to the increasing differences arising from increasing sinkage and trim associated with higher Fr in the data.

Table V. Validation for the modified Wigley hull advancing in calm water.

	D	S	$E = D - S$	U_V	S_C	$E_C = D - S_C$	U_V
C_T ($Fr = 0.2$)	4.31×10^{-3}	4.34×10^{-3}	-0.70% D	5.91% D	4.19×10^{-3}	2.78% D	3.02% D
C_T ($Fr = 0.3$)	5.59×10^{-3}	5.65×10^{-3}	-1.07% D	3.78% D	5.50×10^{-3}	1.61% D	2.33% D
C_T ($Fr = 0.4$)	6.26×10^{-3}	6.08×10^{-3}	2.88% D	3.38% D	5.93×10^{-3}	5.27% D	2.08% D

Copyright © 2001 John Wiley & Sons, Ltd.

Figures 6 and 7 show $\zeta_{cp}(x)$ and contours of $\zeta(x, y)$ for all three sets of (Re, Fr). From both $\zeta_{cp}(x)$ and contours of $\zeta(x, y)$, the trends with increasing Fr are evident, i.e. smaller wave amplitude and steepness at lower Fr, and the longer transverse (λ_t) and divergent (λ_d) wavelengths at higher Fr. Also shown is $\zeta_{cp}(x)$ of the standard hull at $Fr = 0.316$, which is similar to that of the modified hull at $Fr = 0.3$, but with slightly longer λ_t due to the higher Fr. The similarity was also observed in C_T and $\zeta(x, y)$ for the modified hull at $Fr = 0.3$ and those

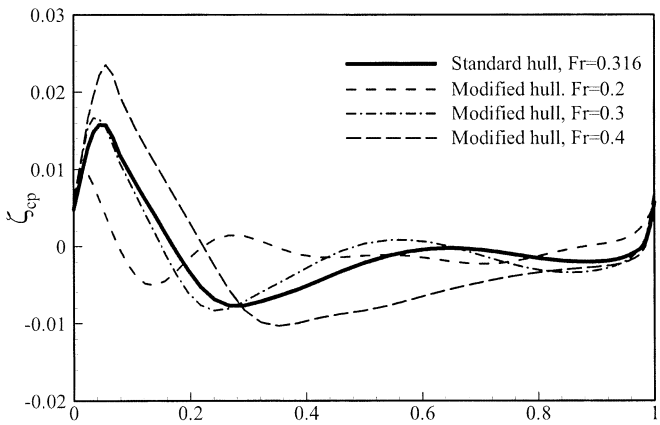

Figure 6. Wave profiles for the modified Wigley hull advancing in calm water.

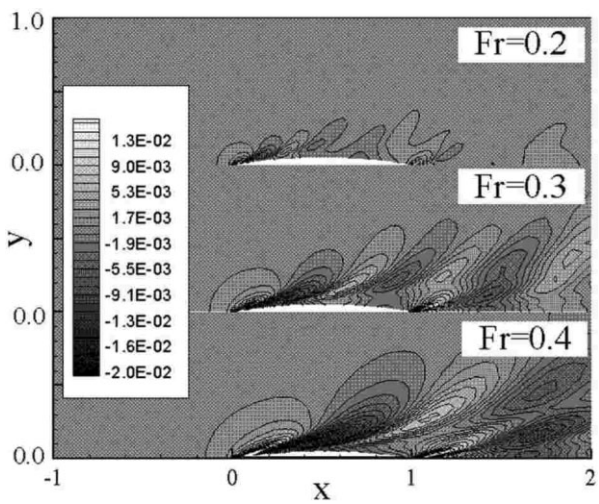

Figure 7. Wave pattern for the modified Wigley hull advancing in calm water.

Copyright © 2001 John Wiley & Sons, Ltd.

for the standard hull at $Fr = 0.316$. Therefore, the effects of the difference in hull forms are not significant between the two hull forms in the present study and, based on that, adopting U_V, U_D, and U_{SN} of the standard hull in the validation for the modified hull can be justified. Also it is noteworthy that the bow wave amplitude is smaller than the incident wave amplitude for LF and MA cases (see A/A_{std} in Table I), which is closely related to the non-linearity in the wave field of a Wigley hull advancing in regular head waves.

6. UNSTEADY FLOW

The steady flow results are comparable to other steady RANS methods in predicting resistance, boundary layer and wake, and free-surface effects. The unsteady flow results cover a wide range of Froude number, wavelength and amplitude, as given in Table I, for which force and moment experimental data are available for validation. Also presented in Table I are A/λ and Ak, which are related to the wave form, and ξ_e and ω_e, which are non-dimensional and dimensional (based on [31]) encounter frequency respectively. ω_e is an important seakeeping parameter, especially when the ship motions in response to incident waves are allowed, and ξ_e is dimensionless and used in the mathematical formulation. Forces and moments, and point variables (surface pressure, free-surface elevations, boundary layer and wake) are discussed in detail for the BASE case followed by overall trends for Fr, λ and A. Comparisons are made with experimental data (forces and moment including validation for the BASE case) and linear potential flow method (forces and moment, surface pressure, and diffraction waves).

The unsteady flow solutions obtained from CFD are $\Phi(t)$, where $\Phi(t)$ is any variable of interest such as hydrodynamic forces and moments, velocity, pressure, wave elevation, and eddy viscosity, etc. $\Phi(t)$ is then post-processed for time and frequency domain analyses. Time domain analysis is based on total response, $\Phi(t)$, unsteady response, $UR(\Phi) = \Phi(t) - \Phi_0$, and unsteady perturbation response, $UPR(\Phi) = \Phi(t) - \Phi_0 - \Phi_{wave}(t)$, where Φ_0 is the zeroth harmonic (time-mean) and $\Phi_{wave}(t)$ represents $\Phi(t)$ of incident waves. $UR(\Phi)$ represents the unsteady response including external flow, while $UPR(\Phi)$ represents the perturbation response to external flow, e.g. diffraction wave. Frequency domain analysis is based on the harmonics, as determined by Fourier series analysis.

Figure 8 shows the time history of F_x, F_z, and M_y of the BASE case. F_x, F_z, and M_y, which are defined in Section 4, are restraining forces and moment for surge, heave, and pitching motions respectively. Also shown are the corresponding frictional and pressure components and time history of the incident wave elevation ζ_e at midship for the discussion on phase relationship. The time history shows a transient state from the initial condition for approximately two periods, which is followed by a predominantly first harmonic response. Also observed are dominant pressure components over frictional ones, which results in the first harmonic amplitude and phase for total forces and moments almost identical to those of the pressure components as evidenced in F_z and M_y.

The harmonic components of F_x, F_z, and M_y of the BASE case are also presented in Figure 8. The zeroth harmonic values are different from steady flow results, i.e. $\Phi_0 = \Phi_{std} + \Phi_{str}$, where Φ_{std} is the corresponding steady flow solution for a Wigley hull advancing in calm water and the difference, Φ_{str}, is steady streaming component. $F_{x,str}$ is added resistance, which is an

Copyright © 2001 John Wiley & Sons, Ltd.

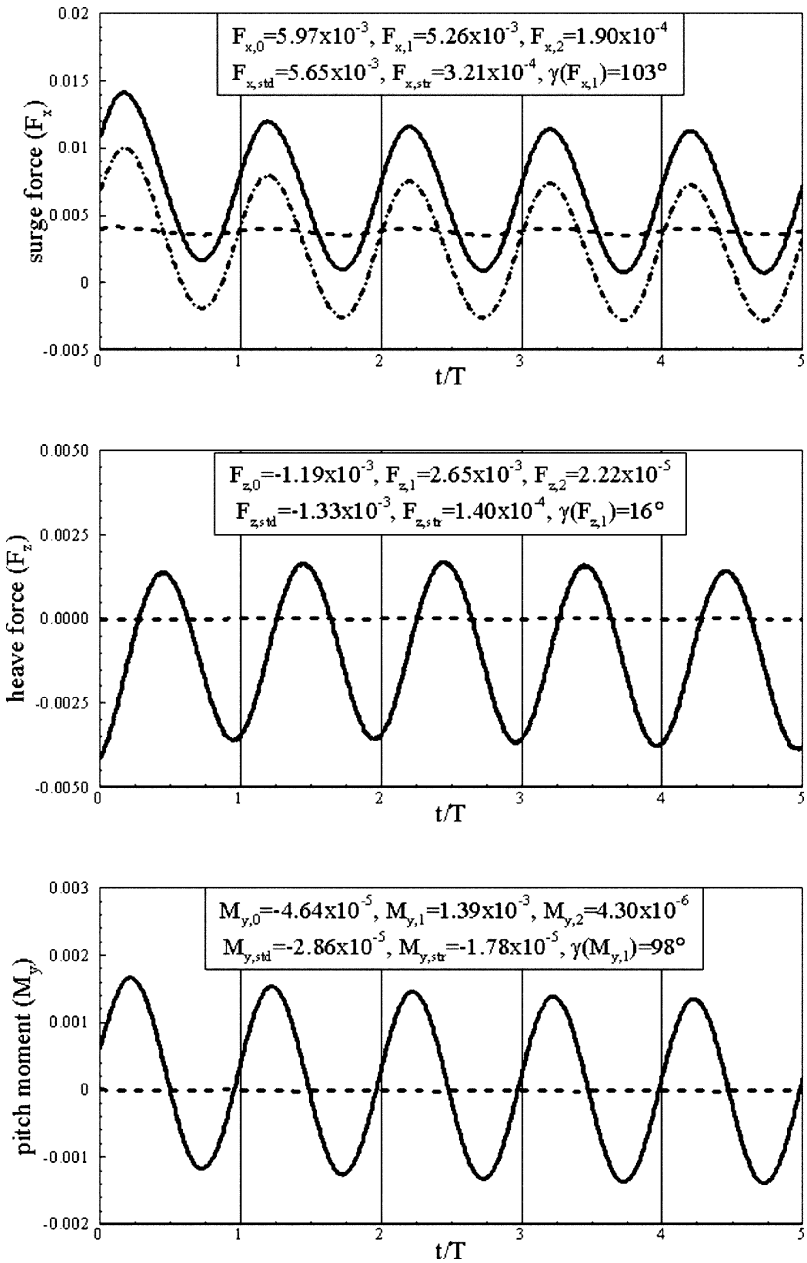

Figure 8. Time history of surge force, heave force, and pitch moment: solid line (total); dashed line (frictional component); dash–dotted line (pressure component); dotted line (incident wave elevation at midship).

Copyright © 2001 John Wiley & Sons, Ltd.

indication of the additional power required in incident waves and will be discussed later for various cases. The first harmonic amplitudes and phases, i.e. $F_{x,1}$, $\gamma(F_{x,1})$, $F_{z,1}$, $\gamma(F_{z,1})$, $M_{y,1}$, and $\gamma(M_{y,1})$, where the subscript '1' denotes the first harmonic component and γ denotes the phase, are largely dependent on the pressure force acting on the hull. Thus, $F_{x,1}$ and $M_{y,1}$ are expected (for $\lambda \geq 1$) to be in phase with the wave crest at forebody shoulder, and $F_{z,1}$ in phase with the wave crest at midship, with approximately 15° phase lead that is obvious in UR(C_p) contours shown later. The 90° lead should be added for $\gamma(F_{x,1})$ and $\gamma(M_{y,1})$, since the phase lead is related to ζ_e at midship, i.e. 90° behind the forebody shoulder. Therefore, $\gamma(F_{x,1})$ is 103°, $\gamma(F_{z,1})$ is 16°, and $\gamma(M_{y,1})$ is 98°. $F_{x,1}/F_{x,\mathrm{std}}$ and $F_{z,1}/F_{z,\mathrm{std}}$ are 0.93 and 1.99 respectively, while $M_{y,1}/M_{y,\mathrm{std}}$ is 48.6, indicating that M_y is the most influenced one by the incident waves. The second harmonic components are at least an order of magnitude smaller than the corresponding first harmonic components.

Table VI presents validation results for $F_{x,1}$, $\gamma(F_{x,1})$, $F_{z,1}$, $\gamma(F_{z,1})$, $M_{y,1}$, and $\gamma(M_{y,1})$ of the BASE case. EFD uncertainty assessment is not available from Journée [31], and U_D is assumed to be 2.5 per cent D for amplitudes and 1.25 per cent 2π for phase as per steady flow validation. Validation is achieved at the level $U_V = 3.34$ per cent D for $F_{x,1}$, 3.18 per cent D for $F_{z,1}$, 6.82 per cent 2π for $\gamma(F_{x,1})$, and 2.69 per cent 2π for $\gamma(M_{y,1})$. Validation is not achieved for $\gamma(F_{z,1})$ and $M_{y,1}$, which show relatively large $|E|$ values, i.e. about 6.84 per cent 2π and 6.11 per cent D respectively. Also presented are error magnitudes of SWAN [11] results. Although SWAN results seem to be comparable for phase predictions, the errors in amplitude predictions are surprisingly (two to ten times) large compared with the present results.

Figure 9(a)–(c) present the trends of $F_{x,1}$, $\gamma(F_{x,1})$, $F_{z,1}$, $\gamma(F_{z,1})$, $M_{y,1}$, and $\gamma(M_{y,1})$ for various cases, including the data [31] and inviscid methods (SWAN and DELTA [44]) for comparison. Also presented are dimensional first harmonic amplitudes, which are based on Journée's experimental condition [31]. The present solutions show good agreement with EFD data [31], and trends are consistent with those of SWAN results. The large errors ($|E|$ larger than 20 per cent D) are observed for LF, which is attributed to the increased non-linearity due to the interaction between short body-generated waves and incident waves.

The non-dimensional first harmonic amplitudes increase with (a) decreasing Fr, (b) increasing λ, and (c) increasing A. The dimensional first harmonic amplitudes, however, slightly increase with Fr, confirming the seakeeping theory that the effects of forward speed on exciting forces are generally small [45]. (b), which also confirms the seakeeping theory, is the most important one with regard to exciting forces and corresponding ship motions (although not

Table VI. Validation of F_x, F_z, and M_y for the BASE case.

	D	S	$\lvert E\rvert$	$\lvert E\rvert$ SWAN	U_V	U_D	U_{SN}
$F_{x,1}$	5.39×10^{-2}	5.26×10^{-2}	2.41% D	16.9% D	3.34% D	2.5% D	2.22% D
$\gamma(F_{x,1})$	109°	103°	1.67% 2π	0.56% 2π	6.46% 2π	1.25% 2π	6.34% 2π
$F_{z,1}$	2.58×10^{-2}	2.65×10^{-2}	2.71% D	26.4% D	3.18% D	2.5% D	1.96% D
$\gamma(F_{z,1})$	41°	16°	6.84% 2π	3.33% 2π	3.65% 2π	1.25% 2π	3.43% 2π
$M_{y,1}$	1.31×10^{-2}	1.39×10^{-2}	6.11% D	13.0% D	3.56% D	2.5% D	2.53% D
$\gamma(M_{y,1})$	99°	98°	0.28% 2π	0.83% 2π	1.61% 2π	1.25% 2π	1.01% 2π

Copyright © 2001 John Wiley & Sons, Ltd.

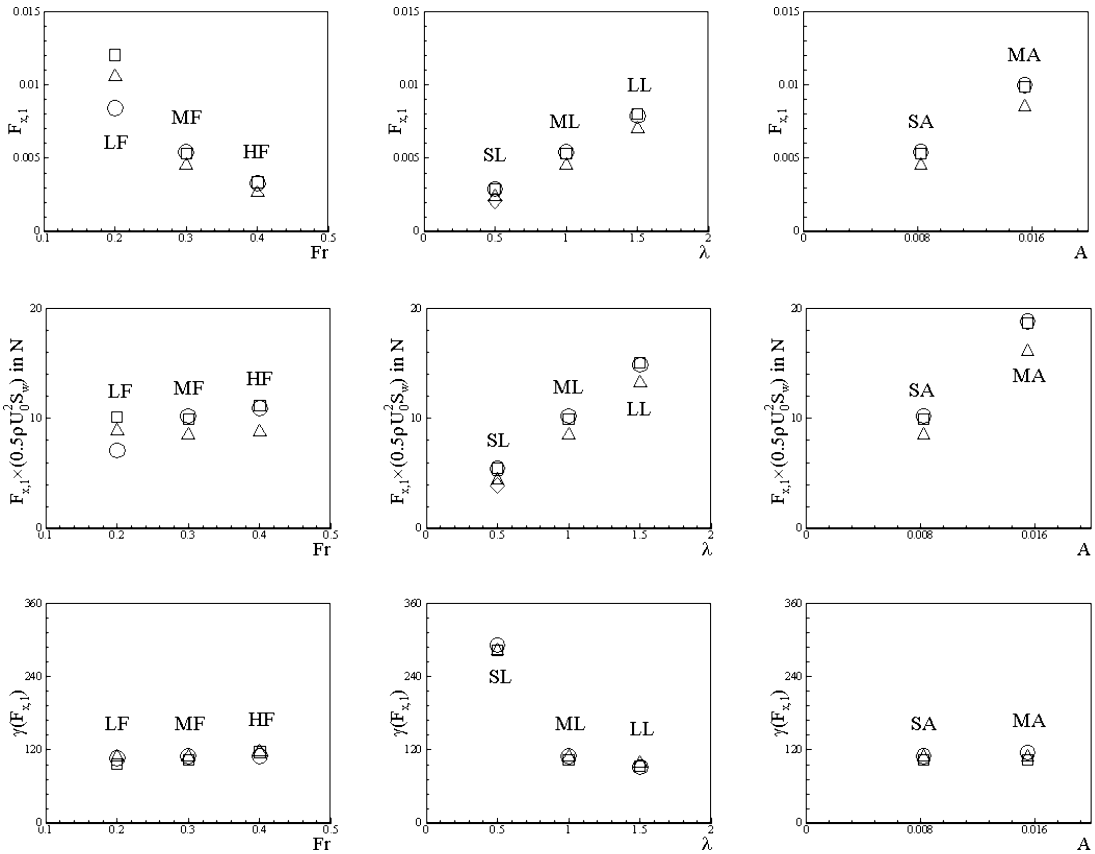

Figure 9. First harmonic amplitude and phases for various cases: circle (Journée, [31]); square (present); triangle (SWAN); diamond (DELTA).

allowed in the present study). (b) is due to the large variation of wetted surface area, which is related to λ, and the cancellation of pressure force along the hull with short incident waves. The present results are limited to short and medium wavelengths and show correct trend of increasing first harmonic amplitude. For larger λ, first harmonic amplitudes decrease such that, in the limit of infinite λ, the first harmonic amplitudes of heave force and pitch moment approach to $\rho g A_w A$ and $\rho g I_L A k$ respectively, where A_w is the waterplane area and I_L the longitudinal moment of inertia of water plane area about the y-axis. This limiting behavior for linear incident waves corresponds to the first harmonic response of pure hydrostatic force and moment when a flat waterline moves up and down across the design waterline of a ship.

The first harmonic phases are nearly unchanged with varying Fr and A, since the wavelength is constant and the pressure force is generally in phase with the incident wave. On the other hand, the first harmonic phases non-linearly decrease with increasing λ due to the large

Copyright © 2001 John Wiley & Sons, Ltd.

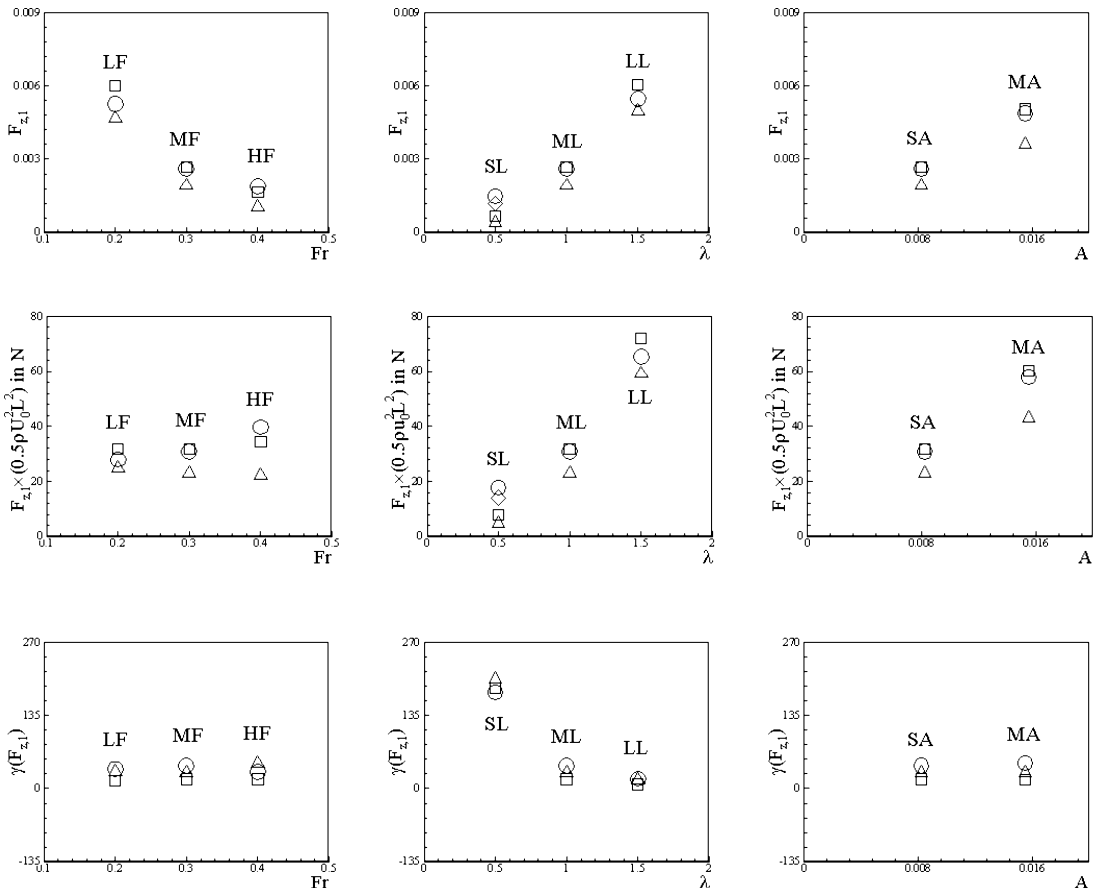

Figure 9 (*Continued*)

variation of wetted surface area with incident waves longer than the ship. The trends of the second harmonic amplitudes are similar to that of the first harmonic amplitudes, but as already noted for the BASE case, second harmonic components are at least one order of magnitude smaller than the corresponding first harmonic components.

Figure 10 shows the added resistance ($F_{x,\mathrm{str}}/F_{x,\mathrm{std}}$) for various cases. EFD data are not available for added resistance from Journée [31]. Usually, added resistance is of concern when the ship motions are allowed in response to the incident waves, so the general conclusions concerning the nature of the added resistance in waves are (a) it is proportional to the square of the wave height, (b) it is independent of calm water resistance, and (c) it would depend on the ship motions and their phase relationship to the wave field [46]. In the present study, however, the ship motions are not allowed, so the general trends are slightly different. The added resistance is between 2 and 10 per cent of steady flow resistance, which is usual for the

Copyright © 2001 John Wiley & Sons, Ltd.

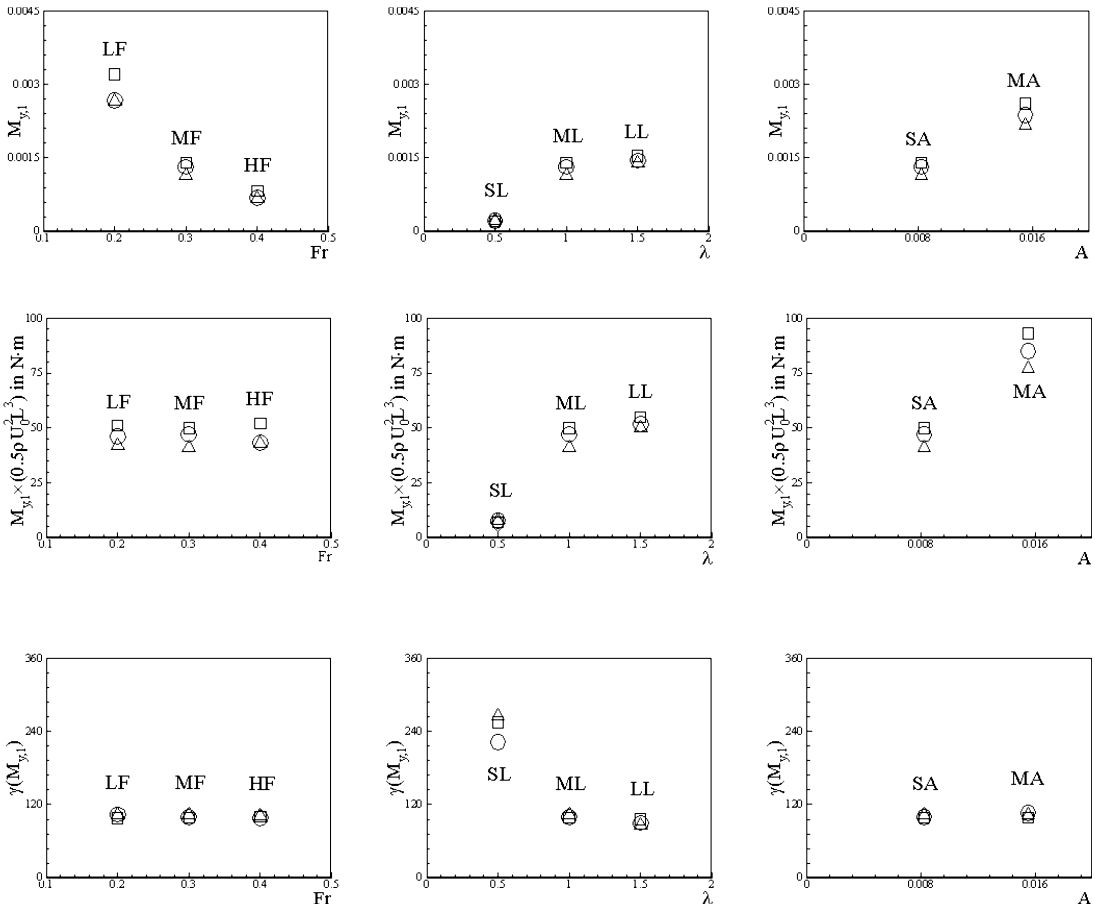

Figure 9 (*Continued*)

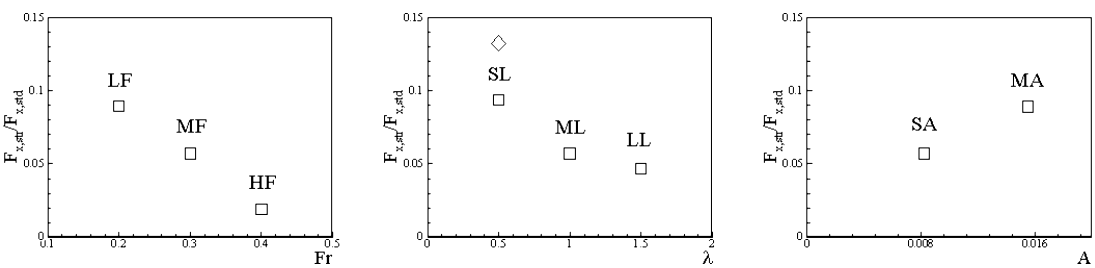

Figure 10. Added resistance ($F_{x,\mathrm{str}}/F_{x,\mathrm{std}}$) for various cases: square (present); diamond (DELTA).

Copyright © 2001 John Wiley & Sons, Ltd.

case with moderate incident waves. The trends of the added resistance are: $F_{x,\mathrm{str}}/F_{x,\mathrm{std}}$ increases with (a) decreasing Fr, (b) decreasing λ, and (c) increasing A. (a) is due to decreasing ω_e with decreasing Fr. (b) is surprising since expectation is for a larger response for smaller ω_e (i.e. longer waves). (c) is a known tendency of the added resistance, although the increase rate is less than A^2.

Figure 11 shows the contours of UR(C_p) of the BASE case, where C_p is the pressure coefficient, by the present method and SWAN at each quarter period (i.e. at $t = 0T$, $T/4$, $T/2$, $3T/4$). UR(C_p) generally follows external flow pressure (see Figure 3) with approximately a 15° phase lead and shows three-dimensional ship geometry effects especially near the bow and stern. Since the global forces and moments are largely dominated by pressure components, the time history of F_x, F_z, and M_y can be related to this figure, such that F_x and M_y are maximum a little before (i.e. approximately a 15° phase lead) $t = T/4$, when the wave crest (maximum pressure force) is at the forebody shoulder, and that F_z is maximum a little before $t = T/2$, when the wave crest is at midship. The overall comparison between the present method and

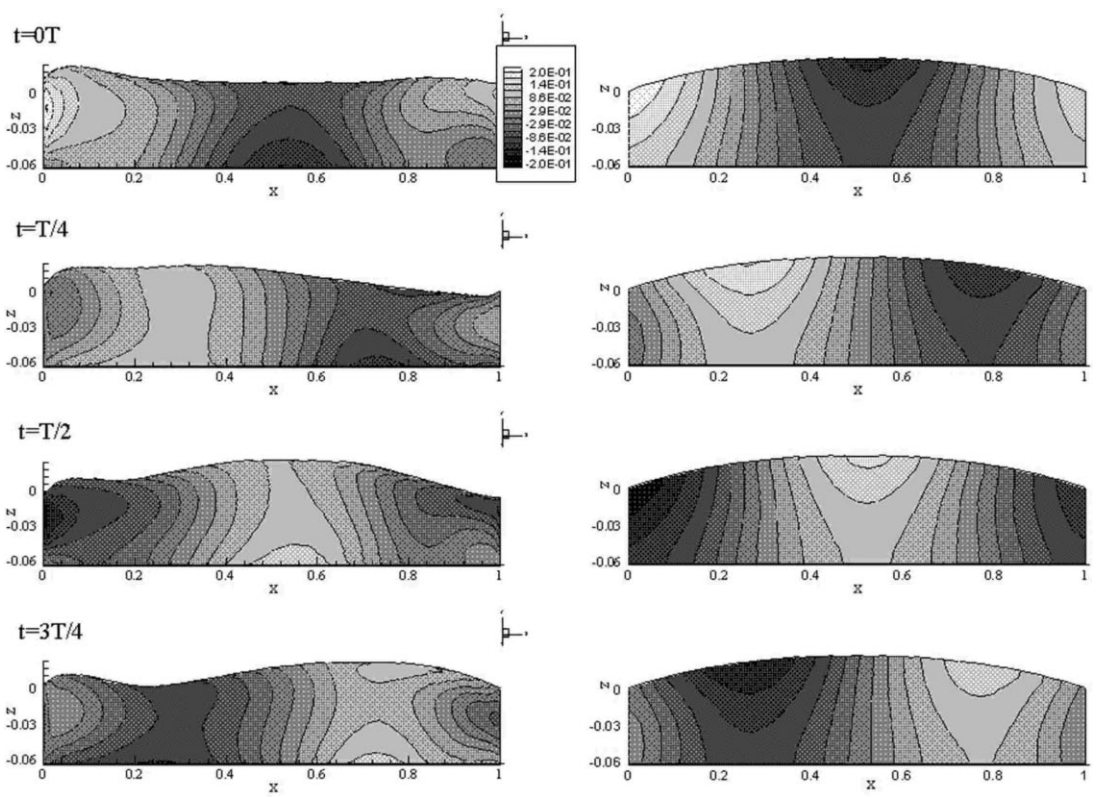

Figure 11. UR(C_p) at each quarter period for the BASE case: present (left); SWAN (right).

Copyright © 2001 John Wiley & Sons, Ltd.

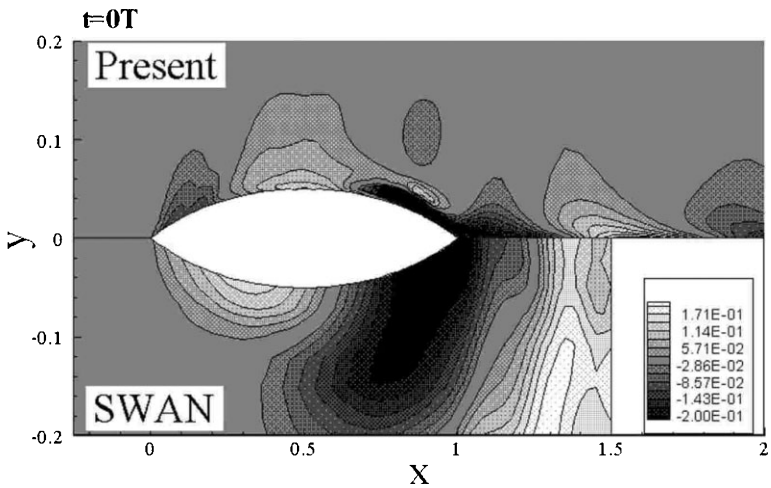

Figure 12. Diffraction wave pattern at $t = 0T$ for the BASE case: present (upper); SWAN (lower).

SWAN is qualitatively good; however, differences that account for the larger errors for restraining forces and moment by SWAN are observed near the bow, stern, and keel, which can be attributed to (a) the difference in wave diffraction which will be shown later, (b) the thick boundary layer at the aft-body, which is critical, but not included in SWAN, (c) the linear superposition of the solutions for three wave potentials (i.e. steady, incident, and diffraction) in SWAN, which cannot include the non-linear interactions between those potentials, and (d) the first-harmonic-only expansion result from the frequency domain solution by SWAN.

Figure 12 shows the contours of diffraction wave of the BASE case normalized by the incident wave amplitude, i.e. UPR(ζ)/A, at $t = 0T$. Also shown is the result by SWAN for comparison. Wave diffraction is the process by which energy spreads laterally to the dominant direction of wave propagation and is considered as a higher-order response of the wave field around a surface-piercing body to incident waves. The main sources of diffraction waves here are bow and stern, and the maximum amplitude and phase shift to the incident waves are approximately 30 per cent of A and a 190° lead respectively, which influence the total wave pattern around the hull and eventually the pressure force acting on the hull surface. Note that, however, the influence of diffraction phenomenon on the forces and moments is not considerably large. The present result is generally consistent with SWAN's. On the hull surface and centerplane, the diffracted wave profiles are comparable to each other, although there are small differences in amplitude and phase, which are also observed in the comparison of UR(C_p) in Figure 11. In the outer region, the present UPR(ζ) seems to be underestimated. For steady flow applications, RANS CFD codes in general underpredict the outer region wave elevations due to numerical dissipation caused by highly stretched meshes, but the present results for the diffraction wave pattern suggest increased dissipation for unsteady flow and improvements may be warranted in the solution procedure for the wave elevation equation.

Copyright © 2001 John Wiley & Sons, Ltd.

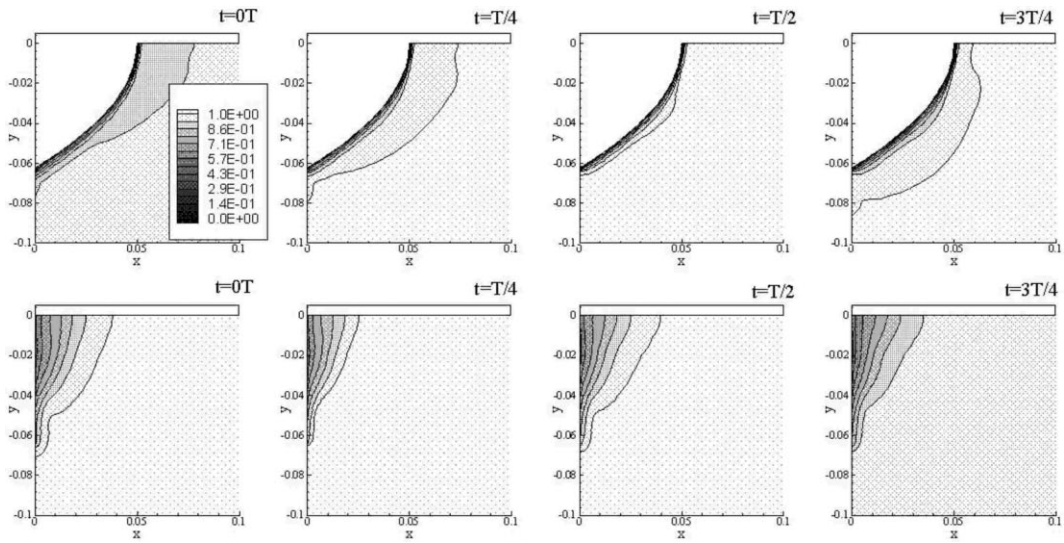

Figure 13. U contours on cross planes at each quarter period for the BASE case: $x = 0.5$ (upper); $x = 1.25$ (lower).

Figure 13 shows contours of U of the BASE case on the cross planes at $x = 0.5$ (upper figures) and $x = 1.25$ (lower figures) at each quarter period. The wave-induced effects are shown as, at $x = 0.5$, acceleration (thinning boundary layer thickness δ) during $0T < t < T/2$, and deceleration (thickening δ) during $T/2 < t < 0T$, and at $x = 1.25$, acceleration (thinning δ) during $3T/4 < t < T/4$, and deceleration (thickening δ) during $T/4 < t < 3T/4$. Also observed is the additional thinning (at $x = 0.5$) and thickening (at $x = 1.25$) δ near the free-surface due to the pressure gradient effects by body-generated waves. Although it is confined in the region very close to the hull surface and therefore difficult to discern, the phase of velocity field is approximately a 30–60° lead to the external flow velocity, which is typical for viscous fluid flow response in high frequency pressure gradient fluctuation, and varies with depth due to the three-dimensional ship geometry. Figure 14 shows the vectors and streamlines of UR(VW) on various cross planes at $t = 0T$. The wave-induced effects, i.e. large amplitude pressure gradient fluctuations, are strong upward and downward W at $x = (0.25, 1.25)$ and $x = (0.75, 1.75)$ respectively, and vortices induced by small and S-shaped W and three-dimensional flow due to the ship geometry at $x = (0.5, 1.0, 1.5)$.

Lastly, the trends of U_0 on the cross plane at $x = 1.0$ with Fr, λ, and A are presented in Figure 15 by showing the zeroth harmonic area of the boundary layer, $A_{\delta,0}$ (normalized by the steady area of the boundary layer $A_{\delta,\mathrm{std}}$). The changes in $A_{\delta,0}$ can be interpreted as the changes in the mean nominal wake in ambient waves, which is crucial information for propeller–hull interaction and eventually the overall resistance and propulsion efficiency of a ship. $A_{\delta,0}$ increases with (a) decreasing Fr (slight increase shown in Figure 15 due to decreasing $A_{\delta,\mathrm{std}}$ for increasing Re), (b) increasing λ, and (c) increasing A. (a) and (b) are due to the decreasing ω_e.

Copyright © 2001 John Wiley & Sons, Ltd.

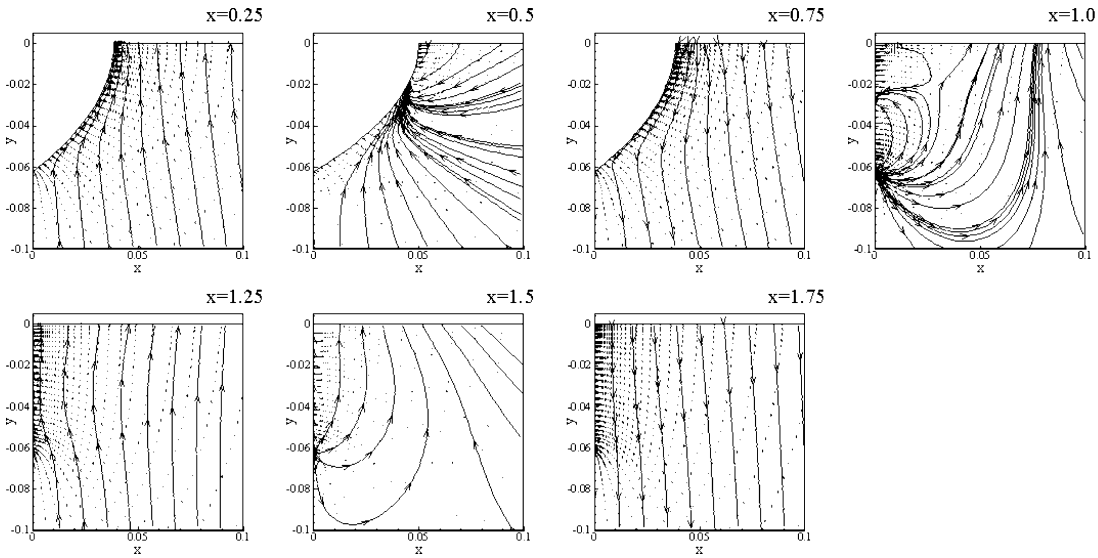

Figure 14. Vectors and streamlines of UR(VW) on cross planes at $t = 0T$ for the BASE case.

(c) may be due to the increasing non-linearity due both to the increasing incident wave steepness (Ak) and increasing amplitude of the external flow velocity, i.e. ξA, on the free-surface.

7. CONCLUDING REMARKS

Results were presented of an unsteady RANS method for simulation of the boundary layer and wake and wave field for a surface ship advancing in regular head waves, but restrained from body motions. Second-order finite differences are used for both spatial and temporal

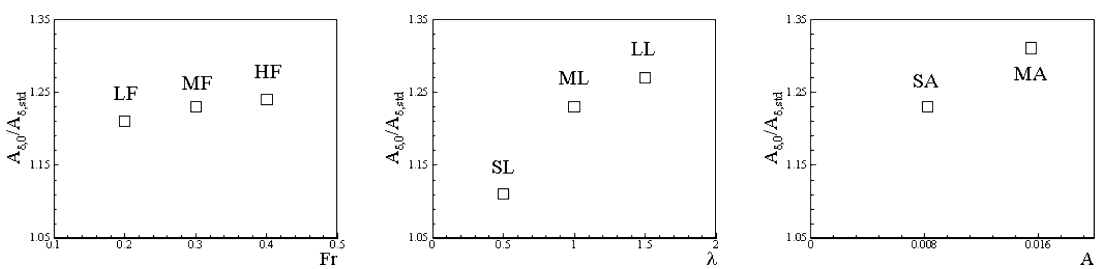

Figure 15. The boundary layer area of zeroth harmonic of U on cross plane at $x = 1.0$.

Copyright © 2001 John Wiley & Sons, Ltd.

discretization and a Poisson equation projection method is used for velocity–pressure coupling. The exact kinematic free-surface boundary condition is solved for the free-surface elevation using a body-fitted/free-surface conforming grid updated in each time step.

The simulations are for the model problem of a Wigley hull advancing in calm water and in regular head waves. Verification and validation procedures are followed, which include careful consideration of both simulation and experimental uncertainties. The steady flow results are comparable to other steady RANS methods in predicting resistance, boundary layer and wake, and free-surface effects. The unsteady flow results cover a wide range of Froude number, wavelength and amplitude for which first harmonic amplitude and phase force and moment experimental data are available for validation along with frequency domain, linear potential flow results for comparisons. The present results, which include the effects of turbulent flow and non-linear interactions, are in good agreement with the data and overall show better capability than the potential flow results. The physics of the unsteady boundary layer and wake and wave field response are explained with regard to frequency of encounter and seakeeping theory.

The results of the present study suggest applicability for additional complexities such as practical ship geometry, ship motion, and maneuvering in arbitrary ambient waves. However, some improvements are warranted and additional experimental data are required. In particular, with regard to the prediction and data for the unsteady diffraction wave field and data for the unsteady boundary layer and wake. The present work was useful in this regard both in guiding future code development efforts [47] and experimental towing tests for validation data [48].

ACKNOWLEDGMENTS

The authors are grateful to Dr. D. Kring at MIT for kindly providing computational results by SWAN. This research was sponsored by the Office of Naval Research under contract N00014-96-1-0018 under the administration of Dr. Ed Rood.

REFERENCES

1. Larsson L, Stern F, Bertram V (eds). *Proceedings of Gothenburg 2000—A Workshop on Numerical Ship Hydrodynamics*. Chalmers University of Technology: Gothenburg, Sweden, 2000.
2. Kodama Y (ed.). *Proceedings of the CFD Workshop Tokyo 1994*. Ship Research Institute: Tokyo, Japan, 1994.
3. Larsson L, Patel VC, Dyne G (ed.). *Proceedings of the 1990 SSPA-CTH-IIHR Workshop on Ship Viscous Flow*. Chalmers University of Technology: Gothenburg, Sweden, 1990.
4. Tahara Y, Longo J, Stern F, Himeno Y. Comparison of CFD and EFD for the Series 60 CB = 0.6 in steady yaw motion. In *Proceedings of the 22nd Symposium on Naval Hydrodynamics*. National Academy Press: Washington, DC, 1998.
5. Alessandrini B, Delhommeau G. Viscous free surface flow past a ship in drift and in rotating motion. In *Proceedings of the 22nd Symposium on Naval Hydrodynamics*. National Academy Press: Washington, DC, 1998.
6. Di Mascio A, Campana EF. The numerical simulation of the yaw flow of a free-surface ship. In *Proceedings of the 7th International Conference on Numerical Ship Hydrodynamics*. Ecole centrale de Nantes: Nantes, France, 1999.
7. Ohmori T. Finite-volume simulation of flows about a ship in maneuvering motion. *Journal of Marine Science and Technology* 1998; **3**(3): 82–93.
8. Beddhu M, Jiang MY, Taylor LK, Whitfield DL. Computation of steady and unsteady flows with a free surface around the Wigley hull. *Applied Mathematics and Computation* 1998; **89**: 67–84.

Copyright © 2001 John Wiley & Sons, Ltd.

9. Gentaz L, Guillerm PE, Alessandrini B, Delhommeau G. Three-dimensional free surface viscous flow around a ship in forced motion. In *Proceedings of the 7th International Conference on Numerical Ship Hydrodynamics*. Ecole Centrale de Nantes: Nantes, France, 1999.
10. Sato Y, Miyata H, Sato T. CFD Simulation of three-dimensional motion of a ship in waves: application to an advancing ship in regular heading waves. *Journal of Marine Science and Technology* 1999; **4**(4): 108–116.
11. Kring D, Huang Y, Sclavounos PD, Vada T, Braathen A. Nonlinear ship motions and wave induced by a Rankine method. In *Proceedings of the 21st Symposium on Naval Hydrodynamics*, Trondheim, Norway, 1996.
12. Ji S, Liu F. Flutter computation of turbomachinery cascades using a parallel unsteady Navier–Stokes code. *AIAA Journal* 1999; **37**(3): 320–327.
13. Paterson EG, Stern F. Computation of unsteady viscous marine-propulsor blade flows—Part 1: validation and analysis. *Journal of Fluids Engineering* 1997; **119**: 145–154.
14. Pierce NA, Alonso JJ. Efficient computation of unsteady viscous flows by an implicit preconditioned multigrid method. *AIAA Journal* 1998; **36**(3): 401–408.
15. Barakos G, Drikakis D. An implicit unfactored method for unsteady turbulent compressible flows with moving boundaries. *Computers and Fluids* 1999; **28**: 899–922.
16. Guilmineau E, Queutey P. Numerical study of dynamic stall on several airfoil sections. *AIAA Journal* 1999; **37**(1): 128–130.
17. Badcock KJ, Cantariti F, Hawkins I, Woodgate M, Dubuc L, Richards BE. Simulation of unsteady turbulent flows around moving aerofoils using the pseudo-time method. *International Journal for Numerical Methods in Fluids* 2000; **32**: 585–604.
18. Gerolymos GA, Vallet I, Bolcs A, Ott P. Computation of unsteady three-dimensional transonic nozzle flows using k–ε turbulence closure. *AIAA Journal* 1996; **34**(7): 1331–1340.
19. Reynier P, Ha Minh H. Numerical prediction of unsteady compressible turbulent coaxial jets. *Computers and Fluids* 1998; **27**: 239–254.
20. Greenblatt D, Damelin SB. Laminar boundary layers subjected to high-frequency traveling wave fluctuations. *AIAA Journal* 1993; **31**(5): 957–959.
21. Choi JE, Sreedhar MK, Stern F. Stokes layers in horizontal-wave outer flows. *Journal of Fluids Engineering* 1996; **118**: 537–545.
22. Dommermuth DG, Yue DKP. A higher-order spectral method for the study of nonlinear gravity waves. *Journal of Fluid Mechanics* 1987; **184**: 267–288.
23. Hirt CW, Nichols BD. Volume of fluid (VOF) method for dynamics of free boundaries. *Journal of Computational Physics* 1981; **39**: 201–225.
24. Hochbaum AC, Vogt M. Flow and resistance prediction for a container ship. In *Proceedings of Gothenburg 2000—A Workshop on Numerical Ship Hydrodynamics*. Chalmers University of Technology: Gothenburg, Sweden, 2000.
25. Rhee SH, Hino T. Unstructured grid flow solver for practical ship hulls. In *Proceedings of Gothenburg 2000—A Workshop on Numerical Ship Hydrodynamics*. Chalmers University of Technology: Gothenburg, Sweden, 2000.
26. Farmer J, Martinelli L, Jameson A. Fast multigrid method for solving incompressible hydrodynamic problems with free surfaces. *AIAA Journal* 1994; **32**(6): 1175–1182.
27. Beddhu M, Taylor LK, Whitfield DL. A time accurate calculation procedure for flows with a free surface using a modified artificial compressibility formulation. *Applied Mathematics and Computation* 1994; **65**: 33.
28. Tahara Y, Stern F. A large-domain approach for calculating ship boundary layers and wakes and wave fields for nonzero Froude number. *Journal of Computational Physics* 1996; **127**: 348.
29. Löhner R, Yang C, Oñate E, Idelssohn S. An unstructured grid-based, parallel free surface solver, 1997. AIAA paper 97-1830.
30. McCarthy JH. Collected experimental resistance component and flow data for three surface ship model hulls, 1985. DTNSRDC-85/011.
31. Journée JMJ. Experiments and calculations on four Wigley hullforms, 1992. Ship Hydromechanics Laboratory, Delft University of Technology, Report No. 909.
32. Stern F, Wilson RV, Coleman HW, Paterson EG. Verification and validation of CFD simulations, 1999. Iowa Institute of Hydraulic Research, Report No. 407.
33. Ekaterinaris JA, Menter FR. Computation of oscillating airfoil flows with one- and two-equation turbulence models. *AIAA Journal* 1994; **32**(12): 2359–2365.
34. Srinivasan, GR, Ekaterinaris JA, McCroskey WJ. Evaluation of turbulence models for unsteady flows of an oscillating airfoil. *Computers and Fluids* 1995; **24**: 833–861.
35. Hytopoulos E, Schetz JA, Simpson RL. Turbulence model for steady and unsteady boundary layers in strong pressure gradients. *Journal of Fluids Engineering* 1997; **119**: 541–549.
36. Wilcox DC. *Turbulence Modeling for CFD* (2nd edn). DCW Ind: La Canada, CA, 1998.

Copyright © 2001 John Wiley & Sons, Ltd.

37. Rhee SH. Unsteady RANS method for surface ship boundary layer and wake and wave field, 1998. Ph.D. thesis, University of Iowa.
38. Harlow FH, Welch JE. Numerical calculation of time-dependent viscous incompressible flow with free-surface. *Physics of Fluids (A)* 1965; **8**: 2182–2187.
39. Sotiropoulos F, Abdallah S. A primitive variable method for the solution of three-dimensional incompressible viscous flows. *Journal of Computational Physics* 1992; **103**: 336.
40. Stern F, Paterson EG, Tahara Y. CFDSHIP-IOWA: computational fluid dynamics method for surface-ship boundary layers, wakes, and wave fields, 1996. IIHR, University of Iowa, Report No. 381.
41. Coleman HW, Stern F. Uncertainties and CFD code validation. *Journal of Fluids Engineering* 1997; **119**: 795–803.
42. Tahara Y, Stern F, Rosen B. An interactive approach for calculating ship boundary layers and wakes for non-zero Froude number. *Journal of Computational Physics* 1992; **98**: 33–53.
43. Longo JF, Stern F. Technical note: evaluation of surface-ship resistance and propulsion model-scale database for CFD validation. *Journal of Ship Research* 1996; **40**: 112–116.
44. Scorpio SM. Fully nonlinear ship-wave computations using a multiple accelerated, desingularized method, 1997. Ph.D. thesis, University of Michigan.
45. Lewis EV (ed.). *Motions in Waves and Controllability*, *Principles of Naval Architecture*, vol. III. The Society of Naval Architecture and Marine Engineers: Jersey City, NJ, 1989.
46. Strom-Tejsen J, Yeh HYH, Moran DD. Added resistance of a ship in a seaway. *Transactions of the Society of Naval Architecture and Marine Engineers* 1973; **81**.
47. Wilson R, Paterson E, Stern F. Unsteady RANS CFD method for naval combatant in waves. In *Proceedings of the 22nd Symposium on Naval Hydrodynamics*, Washington, DC, 1998.
48. Gui L, Longo J, Metcalf B, Shao J, Stern F. Forces and moment and wave pattern for a naval combatant in regular head waves. In *Proceedings of the 23rd Symposium on Naval Hydrodynamics*, Val de Reuil, France, September, 2000.

Copyright © 2001 John Wiley & Sons, Ltd.